Modified propagation of gravitational waves from the early radiation era

Yutong He,[a,b] **Alberto Roper Pol**[c,d,e] **and Axel Brandenburg**[a,b,e,f]

[a]Nordita, KTH Royal Institute of Technology and Stockholm University, Hannes Alfvéns väg 12, 10691 Stockholm, Sweden

[b]The Oskar Klein Centre, Department of Astronomy, Stockholm University, AlbaNova, SE-10691 Stockholm, Sweden

[c]Département de Physique Théorique, Université de Genève, CH-1211 Genève, Switzerland

[d]Université Paris Cité, CNRS, Astroparticule et Cosmologie, Paris, F-75013, France

[e]School of Natural Sciences and Medicine, Ilia State University, 3-5 Cholokashvili Ave, Tbilisi, GE-0194, Georgia

[f]McWilliams Center for Cosmology and Department of Physics, Carnegie Mellon University, 5000 Forbes Ave, Pittsburgh, PA 15213, USA

November 30, 2022

E-mail: yutong.he@su.se, alberto.roperpol@unige.ch, brandenb@nordita.org

Abstract. We study the propagation of cosmological gravitational wave background (GWB) produced by hydromagnetic sources in the early radiation era until the present day. Compared to standard general relativity (GR), we study the effects that parameters of modified theories of gravity, such as the run rate of the effective Planck mass $\alpha_{\rm M}$ and the tensor speed excess $\alpha_{\rm T}$, have on the present-day GW spectrum using numerical simulations beyond the WKB approximation. While $\alpha_{\rm T}$ makes relatively insignificant changes to the GR solution, $\alpha_{\rm M}$ can potentially introduce an enhancement to the spectral slopes of the energy spectrum in the low-frequency regime depending on the chosen time evolution parameterization of $\alpha_{\rm M}$. This effect is additional to the damping or growth occurring equally at all scales that can be predicted by the WKB approximation. We discuss the observational implications in light of the recent observations by pulsar timing array collaborations and future detectors such as SKA, LISA, and DECIGO.

Contents

1 Introduction

The present day Hubble constant, H_0, is measured to be around $H_0 \sim 74\,\mathrm{km/s/Mpc}$ by astrophysical tests using type Ia supernovae [1–3], lensed quasars [4], and megamaser-hosting galaxies [5]. On the other hand, cosmological tests of H_0 constrain its value to $H_0 \sim 67\,\mathrm{km/s/Mpc}$ from cosmic microwave background (CMB) [?] and baryon acoustic oscillations (BAO) [7] experiments, assuming the standard ΛCDM (Λ cold dark matter) model of cosmology. These measurements suggest the presence of a 4–5 σ deviation discrepancy between the early- and late-universe measurements of H_0 [10], known as the Hubble tension. Besides the well-known H_0 tension, a number of other observational discrepancies within the ΛCDM model have been reported, such as the S_8 tension, where $S_8 \propto \sigma_8\,\Omega_{\mathrm{mat},0}^{1/2}$ characterizes the structure growth rate σ_8 and today's matter density $\Omega_{\mathrm{mat},0}$ [11]. A recent summary of over a dozen cosmological tensions and their varied significance can be found in ref. [12].

In view of these tensions, ΛCDM, although being an extremely successful model, does not provide a complete picture and it might be necessary to go beyond it. Since general relativity (GR) is responsible for the gravity sector of ΛCDM, modifying ΛCDM often requires modifying GR. Within the broad subject of modified gravity, a theorem due to Lovelock proves the uniqueness of GR under four assumptions, and therefore provides four general approaches of modifying GR by relaxing each of them. The theorem states that the only

second-order, local gravitational field equations that can be derived from an action containing only the metric tensor in four dimensions are the Einstein field equations (EFEs) [13, 14]. Therefore, modified gravity could be obtained by adding additional fields other than the metric, constructing theories in a dimension other than four, including higher-than-second-order derivatives, or introducing non-locality; see ref. [15] for a comprehensive review on modified gravity.

Among the plethora of modified gravity mechanisms, we focus on scalar-tensor theories and the phenomenological effects in terms of the modified propagation of gravitational waves (GWs) therein. The choice of scalar-tensor theories is due to their versatility. In other words, apart from extending GR by the inclusion of additional fields, they can also be viewed as the four-dimensional effective description of certain higher-dimensional models after a suitable dimensional reduction, or higher-derivative models after reformulation. Therefore, many modified gravity models following three of the four approaches motivated by circumventing Lovelock's theorem can be comprised into scalar-tensor theories. In addition, generic four-dimensional scalar-tensor models with second-order derivatives can be conveniently summarized in the Horndeski class [16? ?]. As a result, Horndeski gravity includes a vast number of different models such as Brans-Dicke [17], quintessence [18], $f(R)$ [19], $f(G)$ [20], k-essence [21], kinetic gravity braiding [22], galileon [23], etc. Moreover, certain subclass within the Horndeski theories has been shown to ease the Hubble tension [26].

At the level of linear perturbation, Horndeski gravity introduces two parameters to the standard GW equation—the tensor speed excess α_T and the running of the effective Planck mass α_M. Although the multimessenger observation of the binary neutron star merger GW170817 and its gamma-ray burst GRB 170817A [24] has put a tight constraint on the speed of GWs, i.e., $\alpha_\mathrm{T} \lesssim \mathcal{O}(10^{-15})$, and therefore the theory space of Horndeski gravity [25], a large number of models of Horndeski gravity remains viable. In fact, this shows the constraining power of GWs as a phenomenological probe. Comparing to α_T, the constraints on α_M are much less stringent. Therefore, in the present work, we focus on exploring α_M and its effects on the energy spectrum of GWs. This subclass of Horndeski theories is also known as reduced Horndeski theories. Specifically, we initialize a GW spectrum based on previous studies of GWs sourced by primordial magnetohydrodynamic (MHD) turbulent fields in the early radiation era—at the electroweak or QCD phase transitions (EWPT or QCDPT)—then propagate it through cosmic history to obtain the present-day relic spectrum. This choice of the GW spectral shape is for convenience but we show that the obtained results can be applied to predict the expected GW spectrum from other sources in reduced Horndeski theories. We then analytically and numerically compare the relic spectra in GR and Horndeski gravity, and discuss their potential observational implications. The numerical solutions in this study are obtained using the Pencil Code [27], which has been a tool for simulations of GWs from primordial turbulent sources since the implementation of a GW solver [28].

Finally, note that an additional propagating degree of freedom (DOF) appears in Horndeski gravity as a consequence of the scalar field. However, we restrict the current study to tensor-mode perturbations, since the amplitude of the scalar mode remains subdominant [29], and the discussions of extra DOFs as a smoking gun for modified gravity overall might deserve a separate study.

We introduce the propagation of tensor-mode perturbations described by the GW equation in modified theories of gravity in section 2. In section 3.1, we introduce the WKB approximation, which is commonly used to describe approximate solutions to the GW equation in modified GR. Then, in section 4, we present some common temporal parameterizations

of the Horndeski parameter α_{M} through the cosmological history of the Universe that have been used in the literature, and we present the numerical simulations that we perform to solve the GW equation using the PENCIL CODE, along with the numerical solutions to the Friedmann equations in section 5. We study, in particular, the additional effect on the GW spectrum that is not found using the WKB approximation. Finally, we discuss potential observational implications of reduced Horndeski theories compared to GR for the different parameterizations of α_{M} in section 6 and conclude in section 7.

Throughout the paper, we set $c = 1$, use the metric signature $(- + ++)$, and define the gravitational coupling constant $\kappa = 8\pi G_{\mathrm{N}}$. We indicate with a prime derivatives with respect to conformal time normalized by the conformal Hubble rate at the time of GW generation $\eta \mathcal{H}_*$ and with a dot derivatives with respect to cosmic time t. Both times are related via the scale factor as $a\, \mathrm{d}\eta = \mathrm{d}t$.

2 Modified GWs on FLRW background

2.1 GW equation in Horndeski theories

The homogeneous and isotropic background is described by the Friedmann-Lemaître-Robertson-Walker (FLRW) metric. Including tensor perturbations, the FLRW line element reads

$$\mathrm{d}s^2 = a^2\big(\mathrm{d}\eta^2 + [\delta_{ij} + a^{-1}h_{ij}(\boldsymbol{x},\eta)]\,\mathrm{d}x^i\,\mathrm{d}x^j\big), \tag{2.1}$$

where $h_{ij} = a h_{ij}^{\mathrm{phys}}$ are the strains obtained by scaling the physical strains h_{ij}^{phys} with the scale factor a. In GR, the GW equation in Fourier space[1] reads [28, 46]

$$\tilde{h}''_{ij}(\boldsymbol{k},\eta) + \left(k^2 - \frac{a''}{a}\right)\tilde{h}_{ij}(\boldsymbol{k},\eta) = \frac{6}{a}\tilde{T}_{ij}^{\mathrm{TT}}(\boldsymbol{k},\eta), \tag{2.3}$$

where $\mathcal{H} \equiv a'/a$ is the conformal Hubble rate normalized by $\mathcal{H}_*$, and an asterisk refers to a reference time in the early universe, e.g., the time at which the GWs were generated. $\tilde{T}_{ij}^{\mathrm{TT}} = \Lambda_{ijlm}\tilde{T}_{lm}$ is the traceless-transverse (TT) projection of the normalized stress energy tensor, i.e., divided by the radiation energy density $\mathcal{E}_{\mathrm{rad}} = 3H^2/\kappa$, being $H \equiv \dot{a}/a$ the Hubble rate at time η. The projection operator is $\Lambda_{ijlm}(\hat{\boldsymbol{k}}) = P_{il}P_{jm} - \frac{1}{2}P_{ij}P_{lm}$, $P_{ij}(\hat{\boldsymbol{k}}) = \delta_{ij} - \hat{k}_i\hat{k}_j$, and $\hat{\boldsymbol{k}} = \boldsymbol{k}/k$. The scale factor at η_* is set to unity, and the wave numbers k are also normalized by the conformal Hubble rate.

In Horndeski gravity [16], the action consists of the metric tensor and an additional scalar field ϕ. Its linear perturbations on the FLRW metric can be characterized by four free parameters separable from the full theory [30]. These free parameters are all arbitrary functions of the scalar field and its kineticity $\nabla_\mu\phi\,\nabla^\mu\phi$. They respectively indicate the following:

- Kineticity α_{K}, indicating the kinetic energy of scalar perturbations.

- Braiding α_{B}, indicating the mixing of the scalar and tensor kineticities.

- Planck-mass run rate α_{M}, denoting the time dependence of the effective Planck mass.

---

[1]We use the Fourier convention

$$\tilde{h}(\boldsymbol{k}) = \int h(\boldsymbol{x})\, e^{-i\boldsymbol{k}\cdot\boldsymbol{x}}\, \mathrm{d}^3\boldsymbol{x}, \quad h(\boldsymbol{x}) = \frac{1}{(2\pi)^3}\int \tilde{h}(\boldsymbol{k})\, e^{i\boldsymbol{k}\cdot\boldsymbol{x}}\, \mathrm{d}^3\boldsymbol{k}. \tag{2.2}$$

- Tensor speed excess α_{T}, measuring the deviation of the speed of gravity from the speed of light.

Out of the four parameters, however, only α_{M} and α_{T} enter and modify the GW equation. As a result, the modifications generalize equation (2.3) to [31]

$$\tilde{h}_{ij}''(\boldsymbol{k}, \eta) + \alpha_{\mathrm{M}} \mathcal{H} \tilde{h}_{ij}'(\boldsymbol{k}, \eta) + \left(c_{\mathrm{T}}^2 k^2 - \alpha_{\mathrm{M}} \mathcal{H}^2 - \frac{a''}{a} \right) \tilde{h}_{ij}(\boldsymbol{k}, \eta) = \frac{6}{a} \tilde{T}_{ij}^{\mathrm{TT}}(\boldsymbol{k}, \eta), \qquad (2.4)$$

where c_{T} denotes the GW propagation speed such that $1 + \alpha_{\mathrm{T}} \equiv c_{\mathrm{T}}^2$, and α_{M} is the run rate of the effective Planck mass M_{eff}^2, parameterized as

$$\alpha_{\mathrm{M}} = \frac{\mathrm{d} \ln M_{\mathrm{eff}}^2}{\mathrm{d} \ln a}. \qquad (2.5)$$

The graviton is massless in Horndeski gravity. However, a massive graviton could be included by adding a $m_{\mathrm{g}} \neq 0$ in equation (2.4) as done in ref. [42] but we omit it in the present work.

2.2 Friedmann equations

In previous works using the PENCIL CODE (see section 5 for more details about the numerical simulations), the simulations are restricted to specific eras, e.g., radiation (RD) or matter domination (MD), using a constant equation of state (EOS), defined to be $w \equiv p/\rho$, being p the pressure and ρ the energy density, such that $w = 1/3$ and 0 during RD and MD, respectively. We also ignored the thermal history of the universe during RD, represented by the relativistic g_* and adiabatic g_{S} DOFs. In GR, the previous formulation is justified since the evolution of the physical strains h_{phys} when the source is inactive ($T_{\sim 0}$) can be approximated to dilute as $h_{\mathrm{phys} \propto a^{-1}}$ if one neglects the evolving relativistic DOFs and transitions between radiation, matter, and dark energy dominations (ΛD) [32]. In the present work, we focus on including such effects and solve the GW equation in modified gravity, which presents richer dynamics even when the source is inactive, from the time of GW generation up to present time.

However, assuming a piece-wise EOS, such that $w = 1/3$, 0, and -1 during RD, MD, and ΛD, respectively, would create discontinuities in the time evolution of $a(\eta)$ and its derivatives needed in equation (2.4). Therefore, to find a smooth $a(\eta)$, we directly solve the Friedmann equations,

$$\frac{\ddot{a}}{a} = -\frac{\kappa}{6} \rho (1 + 3w), \quad \left(\frac{\dot{a}}{a} \right)^2 = \frac{\kappa}{3} \rho, \qquad (2.6)$$

where the dots denote derivatives with respect to cosmic time t. A more convenient form of equation (2.6) can be expressed in terms of the energy density $\Omega(a)$ and a smooth $w(a)$ as

$$\frac{\ddot{a}}{a} = -\frac{1}{2} H_0^2 \Omega(a) [1 + 3w(a)], \quad \left(\frac{\dot{a}}{a} \right)^2 = H_0^2 \Omega(a), \qquad (2.7)$$

where $\Omega(a)$ is defined to be the ratio of total energy density to the present-day critical energy density $\rho_{\mathrm{crit},0} \equiv 3H_0^2/\kappa$, i.e.,

$$\Omega(a) = \frac{\rho(a)}{\rho_{\mathrm{crit},0}} = \Omega_{\mathrm{rad}}(a) + \Omega_{\mathrm{mat}}(a) + \Omega_{\Lambda,0}$$

$$= \left(\frac{a}{a_0} \right)^{-4} \frac{g_*}{g_*^0} \left(\frac{g_{\mathrm{S}}}{g_{\mathrm{S}}^0} \right)^{-\frac{4}{3}} \Omega_{\mathrm{rad},0} + \left(\frac{a}{a_0} \right)^{-3} \Omega_{\mathrm{mat},0} + \Omega_{\Lambda,0}. \qquad (2.8)$$

Numerically we take the present-time values of $\Omega_{\Lambda,0} \simeq 0.684$, $\Omega_{\mathrm{rad},0} \simeq 4.16 \times 10^{-5}\, h^{-2}$, and $\Omega_{\mathrm{mat},0} = 1 - \Omega_{\mathrm{rad},0} - \Omega_{\Lambda,0} \simeq 0.316$, where h takes into account the uncertainties on the present-time Hubble rate $H_0 = 100\, h$ km/s/Mpc. We set $h \simeq 0.67$ for the numerical studies, using the value observed from the CMB, and $g_*^0 \simeq 3.36$ and $g_{\mathrm{S}}^0 \simeq 3.91$ are the reference relativistic and adiabatic DOFs at the present time[2].

The evolution of the relativistic and adiabatic DOFs as a function of the temperature during RD are taken from ref. [?] and expressed as a function of a by taking $a^3 T^3 g_{\mathrm{S}}$ to be constant, following an adiabatic expansion of the universe.

The characteristic EOS, corresponding to the energy density of equation (2.8), can be computed combining equations (2.7) by taking the time derivative of the second equation and introducing the first equation. This yields

$$\frac{\dot{\Omega}(a)}{\Omega(a)} = -3(1+w)\frac{\dot{a}}{a}, \tag{2.9}$$

which allows us to compute $w(a)$ using equation (2.8),

$$w(a) = \left(\frac{1}{3}\Omega_{\mathrm{rad}}(a) - \Omega_{\Lambda,0}\right)\Omega^{-1}(a). \tag{2.10}$$

Equation (2.9) justifies the expected evolution of $\Omega(a)$ used in equation (2.8): approximately proportional to a^{-4} during the RD era, to a^{-3} during the MD era, and constant during ΛD. During RD, the evolution of DOFs induces some modifications with respect to the a^{-4} evolution. In the transition between different eras, $\Omega(a)$ evolves smoothly among the asymptotic behaviors. Equation (2.10) yields $w = 1/3$ for RD, $w = 0$ for MD, and $w = -1$ for ΛD, as expected. In the intermediate times, the function $w(a)$ transitions smoothly. With equations (2.8) and (2.10) explicitly in terms of a, we can compute the relevant quantities that appear in the modified GW equation (2.4), given in equation (2.7), and expressed in terms of the normalized conformal time $\eta \mathcal{H}_*$ as

$$\mathcal{H} = \frac{aH_0}{\mathcal{H}_*}\sqrt{\Omega(a)}, \quad \frac{a''}{a} = \frac{1}{2}\mathcal{H}^2\big[1 - 3w(a)\big], \tag{2.11}$$

where the term $\mathcal{H}_*$ appears due to our definition of the normalized $\mathcal{H} = a'/a$, and we set $a_* = 1$ for consistency with our GW equation; see discussion below equation (2.3). Finally, since equation (2.4) is expressed in terms of conformal time η but equation (2.11) is still written in terms of a, we would like to substitute the variables via $a(\eta)$, which can be obtained using equation (2.7):

$$\dot{a} = H_0\, a\sqrt{\Omega(a)} \Rightarrow \mathrm{d}(H_0 t) = \frac{\mathrm{d}a}{a\sqrt{\Omega(a)}} \Rightarrow H_0(t - t_{\mathrm{ini}}) = \int_{a_{\mathrm{ini}}}^a \frac{\mathrm{d}a}{a\sqrt{\Omega(a)}}. \tag{2.12}$$

This allows us to compute $t(a)$ and then invert the relation to obtain $a(t)$. Similarly, in conformal time we have $\mathrm{d}t = a\,\mathrm{d}\eta$, so we solve

$$H_0(\eta - \eta_{\mathrm{ini}}) = \int_{a_{\mathrm{ini}}}^a \frac{\mathrm{d}a}{a^2\sqrt{\Omega(a)}}. \tag{2.13}$$

---

[2]Note that neutrinos' contribution to the radiation energy density is accounted for by taking $g_*^0 \simeq 3.36$, instead of $g_*^0 = 2$ at the present day due to photons only. This leads to an excess in the calculation of the radiation energy density after neutrinos become massive. However, this occurs when the radiation energy is subdominant and hence, it does not affect our calculations.

For the numerical integration, we set $a_{\text{ini}} = 10^{-20}$ at $t_{\text{ini}} = \eta_{\text{ini}} = 0$, which yields accurate results for all $a \gtrsim 10^{-19}$.

In the present work, we consider that the GWs are generated during a phase transition (in particular, at the EWPT or QCDPT) within the RD era. Assuming adiabatic expansion of the universe, one can compute a_*/a_0 as a function of the temperature T_* and the adiabatic DOFs,

$$\frac{a_*}{a_0} \simeq 7.97 \cdot 10^{-16} \frac{T_*}{100\ \text{GeV}} \left(\frac{g_{\text{S}}}{100} \right)^{-\frac{1}{3}}. \tag{2.14}$$

Setting $a_* = 1$, such that $\mathcal{H}_* = H_*$, this gives a value of the Hubble rate (valid during the RD era),

$$\mathcal{H}_* = 2.066 \cdot 10^{10}\ \text{Hz} \left(\frac{T_*}{100\ \text{GeV}} \right)^2 \left(\frac{g_*}{100} \right)^{\frac{1}{2}}, \tag{2.15}$$

with $\eta_* = \mathcal{H}_*^{-1}$. These results allow us to use the solutions from Friedmann equations and adapt them to compute the variables that appear in equation (2.4), normalized to the specific epoch of GW generation.

3   WKB approximation

3.1   Solution of the GW equation

Modifications of the GW propagation, in the absence of sources[3] (i.e., $T_{ij} = 0$), have been studied using the WKB approximation [33, 34]. The WKB solution can be obtained using the following ansatz

$$\tilde{h}_{ij}(k, \eta) = h(k, \eta)\, e_{ij} = A e_{ij}\, e^{iB}, \tag{3.1}$$

where A and B are generic coefficients, and e_{ij} is the polarization tensor.[4] Substituting this into equation (2.4), one gets

$$2\frac{A'}{A} + \frac{B''}{B'} + \alpha_{\text{M}}\mathcal{H} = 0 \Rightarrow A(\eta) = e^{-\mathcal{D}}, \tag{3.2}$$

$$B'^2 = \frac{A''}{A} + \alpha_{\text{M}}\mathcal{H}\frac{A'}{A} + c_{\text{T}}^2 k^2 - \alpha_{\text{M}}\mathcal{H}^2 - \frac{a''}{a} \approx c_{\text{T}}^2 k^2 \Rightarrow B = \pm k(\eta\mathcal{H}_* - \Delta T), \tag{3.3}$$

where, following the WKB approximation, we neglect the terms A''/A, A'/A, $\mathcal{H}^2$, and a''/a, when compared to $c_{\text{T}}^2 k^2$. In addition, we also neglect the term $B''/B' \sim c'_{\text{T}}/c_{\text{T}} \sim 0$. We have defined the damping factor $\mathcal{D}$ and the time delay due to the effective GW speed ΔT that appear in theories of modified gravity [33]

$$\mathcal{D}(\eta) = \frac{1}{2} \int_1^{\eta\mathcal{H}_*} \alpha_{\text{M}}\mathcal{H}\, d\eta', \quad \Delta T(\eta) = \int_1^{\eta\mathcal{H}_*} (1 - c_{\text{T}})\, d\eta'. \tag{3.4}$$

Hence, the solution is

$$h(k, \eta) = e^{-\mathcal{D}} e^{\pm ik(\eta\mathcal{H}_* - \Delta T)} = e^{-\mathcal{D} \mp ik\Delta T} h^{\text{GR}}(k, \eta), \tag{3.5}$$

---

[3]In the absence of sources, the GW equation [see equation (2.4)] does not depend on the wave vector $\boldsymbol{k}$ but only on its modulus (the wave number) k. Hence, the solution can simply be expressed as a function of k.

[4] In the absence of sources, the GW propagation of any polarization mode is the same, so we can just call h the amplitude of each mode. If the produced GW signal is polarized, then for each mode we need to impose the corresponding initial conditions.

where $\mathcal{D} = \Delta T = 0$ in GR. For the initial conditions[5] $h(k, \eta_*) = h_*(k)$ and $h'(k, \eta_*) = h'_*(k)$, we get

$$h(k, \eta) = e^{-\mathcal{D}} \left[h_*(k) \cos k(\eta \mathcal{H}_* - 1 - \Delta T) + \frac{h'_*(k) + \frac{1}{2}\alpha_{\mathrm{M}}^* h_*(k)}{kc_{\mathrm{T}}} \sin k(\eta \mathcal{H}_* - 1 - \Delta T) \right],$$

$$= e^{-\mathcal{D}} \left[h_*(k) \cos k \, \tilde{c}_{\mathrm{T}}(\eta \mathcal{H}_* - 1) + \frac{h'_*(k) + \frac{1}{2}\alpha_{\mathrm{M}}^* h_*(k)}{kc_{\mathrm{T}}} \sin k \, \tilde{c}_{\mathrm{T}}(\eta \mathcal{H}_* - 1) \right], \qquad (3.6)$$

where $\alpha_{\mathrm{M}}^* = \alpha_{\mathrm{M}}(\eta_*)$ and $\tilde{c}_{\mathrm{T}}(\eta) = \int c_{\mathrm{T}} \, \mathrm{d}\eta' / (\eta \mathcal{H}_* - 1)$. Note that the specific choice of initial conditions does not allow to give a linear relation between h and h^{GR} as done in ref. [33] and, in general, $h \neq e^{-\mathcal{D} - ik\Delta T} h^{\mathrm{GR}}$, which is only true when referring to the particular solution of the ODE, given in equation (3.5). This reduces to the solution in GR when $c_{\mathrm{T}} = 1$ and $\alpha_{\mathrm{M}} = 0$,

$$h^{\mathrm{GR}}(k, \eta) = h_*(k) \cos k(\eta \mathcal{H}_* - 1) + \frac{h'_*(k)}{k} \sin k(\eta \mathcal{H}_* - 1). \qquad (3.7)$$

In reduced Horndeski theories with $\alpha_{\mathrm{T}} = 0$, the WKB solution yields

$$\tilde{h}_{ij}(k, \eta) = e^{-\mathcal{D}} \left[\tilde{h}_{ij}^{\mathrm{GR}}(k, \eta) + \frac{1}{2} e_{ij} \frac{\alpha_{\mathrm{M}}^* h_*(k)}{k} \sin k(\eta \mathcal{H}_* - 1) \right]. \qquad (3.8)$$

When $\alpha_{\mathrm{M}} = 0$ and c_{T} is a constant in time we find

$$\tilde{h}_{ij}(k, \eta) = h_*(k) \cos \left[c_{\mathrm{T}} k (\eta \mathcal{H}_* - 1) \right] + \frac{h'_*(k)}{kc_{\mathrm{T}}} \sin \left[c_{\mathrm{T}} k (\eta \mathcal{H}_* - 1) \right]. \qquad (3.9)$$

3.2 Limitations of the WKB approximation

To obtain the WKB solution we have neglected some terms in equation (3.3) that would otherwise appear in the solution. These terms can be expressed in the following way

$$\frac{A''}{A} + \alpha_{\mathrm{M}} \mathcal{H} \frac{A'}{A} - \alpha_{\mathrm{M}} \mathcal{H}^2 - \frac{a''}{a} = -\frac{1}{2}\alpha_{\mathrm{M}} \left(1 + \frac{1}{2}\alpha_{\mathrm{M}} \right) \mathcal{H}^2 - \frac{1}{2}\alpha'_{\mathrm{M}} \mathcal{H} - \frac{a''}{a} \left(1 + \frac{1}{2}\alpha_{\mathrm{M}} \right), \qquad (3.10)$$

where we have used $\mathcal{H}' = a''/a - \mathcal{H}^2$. Hence, the WKB assumption could break down when at least one of these terms is not negligible when compared to $k^2 c_{\mathrm{T}}^2$. We have one term that depends on α_{M}, one term that depends on the time evolution of α_{M}, and one term that depends on a''/a. The latter appears also in GR when WKB is used to approximate the solution for the scaled strains, which do not decay (note that the decay of the physical strains is already absorbed by the scale factor), as shown in equation (3.7). This term is given in equation (2.11) and its upper bound can be found using Friedmann equations (using $h = 0.67$),

$$\frac{a''}{a} \leq \frac{1}{2} \frac{\Omega_{\mathrm{mat},0}}{\Omega_{\mathrm{rad},0}} \frac{g_*}{g_*^0} \left(\frac{g_{\mathrm{S}}}{g_{\mathrm{S}}^0} \right)^{-\frac{4}{3}} \mathcal{H} \frac{a_*}{a_0} \lesssim 4.5 \times 10^3 \, \mathcal{H} \frac{a_*}{a_0}, \qquad (3.11)$$

where the first inequality is an approximated value valid during the RD era and it decays during MD. Hence, the upper bound is valid at all times and its specific value depends on

---

[5]In the current work, we focus on the propagation of a GW background after it has already been generated and reached a stationary solution, and the source is no longer active. Since the propagation only depends on k, the initial conditions can be computed from the 3D fields in Fourier space, after shell integration over directions $\hat{\boldsymbol{k}}$, for each polarization mode.

a_*/a_0. For example, for GWs generated at the EWPT or at the QCDPT, this leads to the following critical wave numbers, at which the WKB approximation might break down,

$$k_{\lim, a''}^{\mathrm{EW}} \sim 1.87 \cdot 10^{-6} \, \mathcal{H} \sqrt{\frac{\left|1 + \frac{1}{2}\alpha_{\mathrm{M}}\right|}{c_{\mathrm{T}}}} \leq 1.87 \cdot 10^{-6} \sqrt{\frac{\left|1 + \frac{1}{2}\alpha_{\mathrm{M}}\right|}{c_{\mathrm{T}}}}, \qquad (3.12)$$

$$k_{\lim, a''}^{\mathrm{QCD}} \sim 5.90 \cdot 10^{-5} \, \mathcal{H} \sqrt{\frac{\left|1 + \frac{1}{2}\alpha_{\mathrm{M}}\right|}{c_{\mathrm{T}}}} \leq 5.90 \cdot 10^{-5} \sqrt{\frac{\left|1 + \frac{1}{2}\alpha_{\mathrm{M}}\right|}{c_{\mathrm{T}}}}. \qquad (3.13)$$

In both cases, this term is subdominant up to very large superhorizon scales and it is bounded by the values in equations (3.12) and (3.13) since $\mathcal{H} = \eta_*/\eta$ during RD era as can be seen using equation (2.11). This limit can be modified by the inclusion of α_{M} and α_{T} but unless they take large values these modifications are negligible.

On the other hand, two additional limitations to the WKB approximation appear due to the α_{M} parameter,

$$k_{\lim, \alpha_{\mathrm{M}}} \sim \frac{\mathcal{H}}{c_{\mathrm{T}}} \sqrt{\left|\frac{\alpha_{\mathrm{M}}}{2}\left(1 + \frac{1}{2}\alpha_{\mathrm{M}}\right)\right|} \lesssim \frac{1}{c_{\mathrm{T}}}\sqrt{\frac{|\alpha_{\mathrm{M}}|}{2}}, \quad k_{\lim, \alpha'_{\mathrm{M}}} \sim \frac{\mathcal{H}}{c_{\mathrm{T}}}\sqrt{\frac{|\alpha'_{\mathrm{M}}|}{2}} \leq \frac{1}{c_{\mathrm{T}}}\sqrt{\frac{|\alpha'_{\mathrm{M}}|}{2}}, \quad (3.14)$$

where we can neglect the term $\frac{1}{2}\alpha_{\mathrm{M}}$ in front of 1 in the first limit for small values of α_{M}. Hence, the WKB limit can break down in Horndeski theories around the horizon or at larger scales. In general, we expect the limit from α_{M} to be more restrictive than that from α'_{M} and to dominate at the initial time when $\mathcal{H} = 1$. However, this depends on the parameterization of α_{M}, which can give different results for both limits; see section 4.

3.3 GW spectrum using the WKB approximation

The spectrum of GW energy density can be expressed as

$$\Omega_{\mathrm{GW}}(k, \eta) = \frac{1}{\rho_{\mathrm{crit},0}} \frac{\mathrm{d}\ln\rho_{\mathrm{GW}}}{\mathrm{d}\ln k} = \frac{1}{6}\left(\frac{H_*}{H_0}\right)^2\left(\frac{a_*}{a_0}\right)^4 k S_{h'}(k, \eta), \qquad (3.15)$$

where $2S_{h'}$ is the spectrum[6] of the scaled strain derivatives,

$$\langle \tilde{h}'_{ij}(\boldsymbol{k}, \eta)\, \tilde{h}'_{*}(\boldsymbol{k}', \eta)\rangle = (2\pi)^6 \delta^3(\boldsymbol{k} - \boldsymbol{k}') \frac{2S_{h'}(k, \eta)}{4\pi k^2}, (3.17)$$

and it can be computed using the WKB approximation. Taking $\mathcal{D}' = \frac{1}{2}\alpha_{\mathrm{M}}\mathcal{H}$, the modified GW energy spectrum can be obtained using the WKB solution for reduced Horndeski theories, given in equation (3.8),

$$\Omega_{\mathrm{GW}}(k, \eta) = e^{-2\mathcal{D}}\Omega_{\mathrm{GW}}^{\mathrm{GR}}(k, \eta)$$
$$\times \left(1 + \frac{1}{2}\alpha_{\mathrm{T}} + \frac{\alpha_{\mathrm{M}}^{*\,2}\alpha_{\mathrm{M}}^2\mathcal{H}^2}{32k^4c_{\mathrm{T}}^2} + \frac{\alpha_{\mathrm{M}}^*\alpha_{\mathrm{M}}^2\mathcal{H}^2}{8k^3c_{\mathrm{T}}^2} + \frac{1}{8k^2}\left[\alpha_{\mathrm{M}}^2\mathcal{H}^2\left(1 + \frac{1}{c_{\mathrm{T}}^2}\right) + \alpha_{\mathrm{M}}^{*\,2}\right] + \frac{\alpha_{\mathrm{M}}^*}{2k}\right). \quad (3.18)$$

---

[6] Following ref. [28], we define the spectrum $S_{h'}(k, \eta)$ from the $+$ and $\times$ polarization modes, giving an extra factor of 2 due to the property

$$\tilde{h}'_{ij}(\boldsymbol{k}, \eta)\, \tilde{h}'^*_{ij}(\boldsymbol{k}, \eta) = 2\left[h'_+(\boldsymbol{k}, \eta)\, h'^*_+(\boldsymbol{k}, \eta) + h'_\times(\boldsymbol{k}, \eta)h'^*_\times(\boldsymbol{k}, \eta)\right]. \qquad (3.16)$$

At late times, $\mathcal{H}^2 = (\eta_*/\eta)^2$ decreases, so we can neglect the terms that dilute with $\mathcal{H}^2$,

$$\Omega_{\mathrm{GW}}(k, \eta \gg \eta_*) = \tfrac{1}{2} e^{-2\mathcal{D}} \Omega_{\mathrm{GW}}^{\mathrm{GR}}(k, \eta) \left[1 + \alpha_{\mathrm{T}} + \left(1 + \frac{\alpha_{\mathrm{M}}^*}{2k} \right)^2 \right]. \qquad (3.19)$$

From equation (3.19), we can identify the IR and UV limiting ranges of the spectrum,

$$\Omega_{\mathrm{GW}}^{\mathrm{IR}} = \Omega_{\mathrm{GW}} \left(k \ll \tfrac{1}{2} \alpha_{\mathrm{M}}^*, \eta \gg \eta_* \right) = \frac{\alpha_{\mathrm{M}}^{*\,2}}{8k^2} e^{-2\mathcal{D}} \Omega_{\mathrm{GW}}^{\mathrm{GR}}(k, \eta), \qquad (3.20)$$

$$\Omega_{\mathrm{GW}}^{\mathrm{UV}} = \Omega_{\mathrm{GW}} \left(k \gg \tfrac{1}{2} \alpha_{\mathrm{M}}^*, \eta \gg \eta_* \right) = \left(1 + \tfrac{1}{2} \alpha_{\mathrm{T}} \right) e^{-2\mathcal{D}} \Omega_{\mathrm{GW}}^{\mathrm{GR}}(k, \eta). \qquad (3.21)$$

Note that the factor $\alpha_{\mathrm{M}}^{*\,2}$ is part of the IR limit, indicating that the IR enhancement of the form k^{-2} holds regardless of the sign of α_{M}. The critical $k_{\mathrm{crit}} = \tfrac{1}{2} \alpha_{\mathrm{M}}^*$ marks the relative strength of the $\mathcal{O}(k^{-2})$ term in equation (3.19), which means it also indicates where the IR regime begins, i.e., k^{-2} becomes dominant.

Equation (3.18) shows that the GW spectrum in the IR regime can present up to k^{-4} GR spectrum but this and other terms vanish as time evolves since they are proportional to $\mathcal{H}^2$. Hence, at late times, we end up with the GR spectrum amplified by $e^{-2\mathcal{D}}$ at all wave numbers with a k^{-2} enhancement in the IR regime, proportional to the additional $\tfrac{1}{8} \alpha_{\mathrm{M}}^{*\,2}$ factor, as shown in equation (3.19). In the UV regime, we find the $e^{-2\mathcal{D}}$ enhancement and an additional factor $1 + \tfrac{1}{2} \alpha_{\mathrm{T}}$.

We have found that, according to the WKB approximation, the parameter α_{M} introduces changes in the spectral shape at $k \leq k_{\mathrm{crit}} = \tfrac{1}{2} \alpha_{\mathrm{M}}^*$ that do not dilute as time evolves and depend on the value of α_{M} only at the time of GW generation. On the other hand, note that, using equation (3.14), the WKB approximation breaks down at $k \sim \max(k_{\mathrm{lim}, \alpha_{\mathrm{M}}}, k_{\mathrm{lim}, \alpha_{\mathrm{M}}'})$. This means that when $\mathcal{H} \sim 1$, the spectral changes occur at wave numbers around and below the critical k_{crit}, where the WKB approximation might not be valid (for $c_{\mathrm{T}} \sim 1$).

Finally, we note that α_{T} introduces no changes to the spectral shape. Instead, its impact corresponds to an enhancement or depletion of the GW spectrum by a factor

$$\Delta\Omega_{\mathrm{GW}}(k, \eta \gg \eta_*) = \frac{\Omega_{\mathrm{GW}} - \Omega_{\mathrm{GW}}^{\mathrm{GR}} e^{-2\mathcal{D}}}{\Omega_{\mathrm{GW}}^{\mathrm{GR}} e^{-2\mathcal{D}}} = \tfrac{1}{2} \left[\alpha_{\mathrm{T}}(\eta) + \frac{\alpha_{\mathrm{M}}^*}{k} + \frac{\alpha_{\mathrm{M}}^{*\,2}}{4k^2} \right], \qquad (3.22)$$

which includes the increase on amplitude from α_{M} via the damping factor $\mathcal{D}$. Note that we define the increase on $\Omega_{\mathrm{GW}}(k)$ after compensating $\Omega_{\mathrm{GW}}^{\mathrm{GR}}$ by $e^{-2\mathcal{D}}$ to see the additional effects of $\alpha_{\mathrm{M}} \neq 0$ on the spectral shape and the change in amplitude due to $\alpha_{\mathrm{T}} \neq 0$. The sign of α_{T} determines if the GW spectrum is amplified or decreased with respect to that obtained from GR.

We investigate the resulting spectra in modified GR using numerical simulations in section 5 with the objective to test the validity of the WKB approximation and its potential limitations and to confirm the resulting GW spectra when Horndeski parameters are introduced due to modified theories of gravity.

4 Phenomenological parameterizations

In Sec. 3.3, we noted that, according to the WKB approximation, $\alpha_{\mathrm{T}} \neq 0$ induces modifications in the total GW energy density, but not in its spectral shape. Realistically, the tensor speed excess at the present day is observationally constrained to be $\alpha_{\mathrm{T},0} \lesssim \mathcal{O}(10^{-15})$ by the

binary neutron star merger GW170817 and its gamma-ray burst GRB 170817A [24]. This constraint can be circumvented if α_{T} is either frequency- or time-dependent, such that larger deviations could hide outside the LIGO-Virgo frequency band [35, 36] or in the past. In this study, we show that even using larger values of α_{T}, constant in time and frequency, the modifications to the GW spectrum are negligible, which is seen from the WKB approximation and can be confirmed with numerical simulations. Hence, from now on, we will focus on two cases: *(i)* constant α_{T} with $\alpha_{\mathrm{M}} = 0$, and *(ii)* reduced Horndeski theories with $\alpha_{\mathrm{T}} = 0$, allowing α_{M} to take different values as a function of time.

In particular, we are interested in the perspectives of negative values of α_{M}, as they would enhance the amplitude of the GW spectrum. Various constraints on the present-day value $\alpha_{\mathrm{M},0}$ exist in the literature, but are significantly less stringent than those on α_{T}. Analytically, $-1.0 \lesssim \alpha_{\mathrm{M},0} \lesssim -0.5$ is found (see figure 4 in [37]). This is compatible with the results from Monte Carlo simulations, giving $|\alpha_{\mathrm{M},0}| \lesssim \mathcal{O}(1)$ (see figure 2 in [34]). On the other hand, the Planck Collaboration reports a constraint on $\alpha_{\mathrm{M},0} \gtrsim -0.1$ (see table 8 of ref. [**?**]). Note that they parameterize $\alpha_{\mathrm{M}} = \alpha_{\mathrm{M},0}\,(a/a_0)^n$ with $n \in (0.5, 1)$. Taking these different constraints into account, we explore a range of $\alpha_{\mathrm{M},0} \in [-0.5, 0.3]$.

Besides the simplest consideration of a constant α_{M} in time, which we call choice 0, its time-dependent forms can be written in accordance with specific gravity models [38]. Following refs. [30, 31, 40], we choose phenomenological forms of α_{M} as simplified parameterizations motivated by effective descriptions of modified gravity [39]. Specifically:

$$\alpha_{\mathrm{M}}(\eta) = \begin{cases} \alpha_{\mathrm{M},0} & \text{(choice 0)}, \\ \alpha_{\mathrm{M},0}\left[\dfrac{a(\eta)}{a_0}\right]^n & \text{(choice I)}, \\ \alpha_{\mathrm{M},0}\dfrac{1}{\Omega(\eta)} & \text{(choice II)}, \\ \alpha_{\mathrm{M},0}\dfrac{1 - \Omega_{\mathrm{mat}}(\eta)/\Omega(\eta)}{1 - \Omega_{\mathrm{mat},0}} & \text{(choice III)}, \end{cases} \tag{4.1}$$

where choices II and III give a value of α_{M} proportional to the percentage of dark energy density and the combination of dark and radiation energy densities, respectively, at each time η compared to their relative amounts at the present time. For choice I, the following conditions on the parameter values are needed in order to ensure the theory's stability [41]:

$$\begin{cases} \alpha_{\mathrm{M},0} > 0 : 0 < n < \tfrac{3}{2}\,\Omega_{\mathrm{mat},0} \simeq \tfrac{1}{2}, \\ \alpha_{\mathrm{M},0} < 0 : n > \tfrac{3}{2}. \end{cases} \tag{4.2}$$

To provide an intuition on the aforementioned α_{M} parameterizations, we show in figure 1 (left panel), for the different time dependencies given in equation (4.1), the evolution of $\alpha_{\mathrm{M}}\mathcal{H}$, which characterizes the growth or damping produced by α_{M}, according to the WKB approximation [see equation (3.4)]. We also show the time evolutions of $\sqrt{\alpha_{\mathrm{M}}}\mathcal{H}$ and $\sqrt{\alpha'_{\mathrm{M}}}\mathcal{H}$ (right panel), which correspond to the wave numbers at which the WKB approximation might break down, according to equation (3.14). Figure 1 shows the time evolution from the time of generation (e.g., EWPT) up to present time. We see that for choices 0 and III, $\alpha_{\mathrm{M}}\mathcal{H}$ converges to the same values during RD and ΛD, and only becomes different during MD, as expected. On the other hand, for choices I and II, $\alpha_{\mathrm{M}}\mathcal{H}$ is negligible for all of RD and most of MD and rapidly increases later on, especially during ΛD. It converges for all parameterizations to
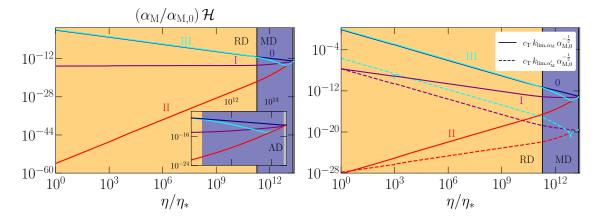
Figure 1: Time evolution of $\alpha_M \mathcal{H}$ (left panel), which contributes to the change of amplitude over time, $h_{ij} \sim e^{-\mathcal{D}}$ with $\mathcal{D} = \frac{1}{2}\int^\eta \alpha_M \mathcal{H}\, d\eta'$, and $k_{\text{lim},\,\alpha_M}/c_T$ and $k_{\text{lim},\,\alpha'_M}/c_T$ (right panel), which are the terms neglected compared to kc_T under the WKB approximation; see equation (3.14). All four parameterization choices (0 to III) are shown and, for illustrative purposes, $n = 1$ is chosen. The main figures show the full evolution whereas the inset (in left panel) shows only times after the onset of matter domination. we show in figure 1, for the different time dependencies. We have taken η_* to correspond to the EWPT for the specific values in the axes, which puts the present time at $\eta_0/\eta_* \simeq 2.38 \times 10^{13}$.

the value $\alpha_{M,0}$ at the present time. We have found in section 3.2 the values of k at which the assumptions made by the WKB approximations do not hold. We see in figure 1 (right panel) that for choices 0 and III, this limiting k is around the horizon scale at the time of generation, i.e., $c_T k_{\text{lim},\,\alpha_M} \sim \sqrt{\alpha_M^*/2}$ and then it decreases into superhorizon scales since it is proportional to $\mathcal{H} = \eta_*/\eta$ (this is because for these choices, $\alpha_M \simeq \alpha_M^*$ during the RD era). The term $\alpha'_M \ll \alpha_M$ for choice III, as can be seen in figure 1. The ratio between α_M and α'_M during the RD era can be found to be

$$\left(\frac{\alpha_M}{\alpha'_M}\right)^{\frac{1}{2}}_{\text{III}} \sim 10^2 \left(\frac{a_*}{a_0}\right)^{\frac{1}{2}} \simeq 3 \times 10^{-6} \left(\frac{a_*}{8 \times 10^{-16}}\right)^{\frac{1}{2}}, \qquad (4.3)$$

which only becomes of order 1 towards the end of the RD era, when $a_*/a_0 \sim 10^{-4}$, which corresponds to times much later than the EWPT and the QCDPT. For choices I and II, although the two terms are of the same order, $\alpha_M^{'*} \sim \alpha_M^*$, their value at the time of GW generation is much smaller than $\alpha_{M,0}$ (for all $n > 0$ in the choice I). For this reason, in these cases the WKB estimate is completely valid and we do not expect to observe any relevant spectral change, since the IR enhancement is determined by the value of α_M^*, as seen in equation (3.22).

Note that, since many efforts of modifying gravity are aimed at addressing the late-time acceleration of the universe, the α_M parameterization choices are commonly constructed to be dominant in the late universe. This is indeed the case for choices I and II here. If one considers only the MD and ΛD history of the universe, choice III is also well-motivated to be relevant at late times. However, here we explore the entire history of the Universe from well within RD, which means that $\alpha_M \mathcal{H}$ becomes dominant for choice III both at early and late times. We note that the physical motivations of the choices here can be potentially ambiguous. Even though there exists a wide range of discussions on modified gravity during

– 11 –

inflation [31?] and around recombination [? ?], where α_M is essentially a free function of the scalar field, there seems to be a relative lack of numerical studies on the effects of α_M during RD (note, however, a brief discussion of $\alpha_M = -1$ during RD in ref. [?]). Hence, we emphasize that the aim of this work is to provide an understanding of the phenomenological behavior of the GW spectrum due to α_M for signals produced during RD.

5 Numerical solutions

To explore the limits and validity of the WKB approximation, we use the PENCIL CODE to numerically solve the GW equation under modified gravity, given in equation (2.4). The PENCIL CODE is a highly parallelized modular code that can be used to solve various differential equations [27]. In the context of cosmological GWs, it has previously been used to study GWs generated by hydrodynamic and MHD stresses in the early universe [?]. It uses a GW solver that advances the strains at each time step sourced by the anisotropic stresses that are separately computed as the solution to the MHD equations [28]. Previous numerical works solved the GW equation under GR, while in the present work, we have extended the code to solve equation (2.4); see appendix A for further details on the numerical scheme.

5.1 Initial condition and time stepping schemes

In the current work, we focus primarily on the propagation rather than the production of GWs. Therefore, we have adapted the PENCIL CODE to evolve an initial GW spectrum in the absence of sources with a spectral shape and amplitude based on those obtained in previous studies (see, e.g., refs. [42, 43]). Hence, equation (2.4) is solved in one-dimension, i.e., in $k > 0$, in order to improve the efficiency of the code to study the propagation of a GW background along the cosmological history of the universe. We take the initial spectrum for the time derivative of the strains to be a smoothed double broken power law described by

$$S_{h'}(k, \eta_*) = S_{h'}^* \frac{2^{\frac{1}{\alpha_2}} \left[1 + \left(\frac{k_*}{k_b} \right)^{a-b} \right] \left(\frac{k}{k_*} \right)^a}{\left[1 + \left(\frac{k}{k_b} \right)^{(a-b)\alpha_1} \right]^{\frac{1}{\alpha_1}} \left[1 + \left(\frac{k}{k_*} \right)^{(b+c)\alpha_2} \right]^{\frac{1}{\alpha_2}}}, \tag{5.1}$$

where $S_{h'}^*$ is approximately the initial peak amplitude, $\eta_* = \mathcal{H}_*^{-1}$ corresponds to the time of GW production during the RD era, and $\alpha_1 = \alpha_2 = 2$ are fixed smoothness parameters. We choose the slope in the IR range to be k^2, set by $a = 2$ (as is expected for causal sources of GWs, as those produced for example during a phase transition) up to the break wave number $k_b = 1$, which corresponds to the horizon scale. At intermediate wave numbers, $k_b \leq k \leq k_*$, the slope becomes $b = 0$, as found, for example, for MHD turbulence in ref. [?] and for sound waves in ref. [?], although in both cases, the break k_b is not exactly at the horizon but depends on the dynamics of the source; see, e.g., ref. [43]. The peak wave number is chosen to be $k_* = 10$, followed by the slope in the UV range as $k^{-\frac{11}{3}}$, set by $c = \frac{11}{3}$. This corresponds to the spectrum obtained for Kolmogorov-like MHD turbulence [?]. Note, however, that this part of the spectrum corresponds to subhorizon scales, which are described accurately by the WKB approximation and, hence, the resulting spectral shape is not expected to be modified in this range. On the other hand, around the horizon or at larger scales, depending on the value of α_M^*, the resulting GW spectral shape might be modified by the inclusion of an additional IR branch $\sim k^{-2} S_{h'}(k)$, as predicted in section 3.3 by the
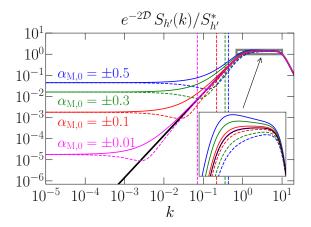
Figure 2: Expected WKB spectrum [see equation (3.19)] of the strain derivatives $S_{h'}(k)$ at late times due to non-zero α_M^* at the time of generation for an initial GW background characterized by a double broken power law, given in equation (5.1). The black curve indicates the GR solution and the colored curves correspond to different values of α_M^*, with the solid and dashed ones being positive and negative values, respectively. Vertical dashed lines indicate the estimated value of $k_{\lim,\alpha_M}$, below which the WKB approximation might break. The inset zooms in on the behaviors around the horizon at $k = k_b = 1$.

WKB approximation. Finally, the resulting spectrum is expected to be enhanced at all wave numbers by a factor $e^{-2\mathcal{D}}(1 + \frac{1}{2}\alpha_T)$ owing to the presence of non-zero Horndeski parameters α_M and α_T in modified gravity. After compensating by this enhancement, which affects equally to all wave numbers, we model the spectral modifications using the function $\xi(k)$, such that $\Omega_{GW}(k) \propto \xi(k)\,\Omega_{GW}^{GR}(k)$ (see table 1). Figure 2 shows the resulting GW spectrum estimated using the WKB approximation for different values of α_M^*. Note, however, that the assumptions made by the WKB approximation break down around the critical wave number at which we expect the relevant spectral modifications.

Table 1 summarizes the input parameters for the numerical studies. The values of $\alpha_{T,0}$ are chosen to be much larger than the current constraints in order to later show the relative insignificance of $\alpha_{T,0}$ even with unrealistically large values. The choices of $\alpha_{M,0}$ are made in line with the limits discussed in section 4.

For series T0 (T0A–T0D), we evolve the solution entirely with increasing time steps, such that $\eta_{next} = \eta_{current}(1 + \delta n_{incr})$ with $\delta n_{incr} = 0.01$, leading to equidistant points in logarithmic time spacing. For series M0 (M0A–M0F), M1 (M1A–M1D), M2 (M2A–M2D), and M3 (M3A–M3F), we keep the nonuniform time scheme during RD and MD but switch to linear time steps during ΛD such that $\eta_{next} = \eta_{current} + \delta\eta$ with $\delta\eta\,\mathcal{H}_* = 5 \times 10^9$. We chose such time evolutions to improve the accuracy of late-time results for reduced Horndeski models, especially the modifications that they present in the IR limit (see last column in table 1). We show in appendix B that decreasing the time step below $\delta\eta\,\mathcal{H}_* = 5 \times 10^9$ does not affect the IR range of the spectra, which indicates that the observed modifications are not due to numerical accuracy. Since series T0 does not exhibit k-dependent modifications, it does not require the additional computational effort. The choice of time schemes and their numerical accuracy is further discussed in appendix B.

In the simulations, we consider the initial time to be the EWPT with a temperature scale $T_* \sim 100\,\text{GeV}$ and the number of relativistic and adiabatic DOFs are $g_S \approx g_* \sim 100$, which

Parameters	Run	$\alpha_{\mathrm{M},0}$	n	$\alpha_{\mathrm{T},0}$	$\Delta\mathcal{E}_{\mathrm{GW}}/\mathcal{E}_{\mathrm{GW}}$	$\xi(k)$
Choice 0	T0A	0	–	-0.5	-2.5×10^{-1}	$k^0\ \forall\ k$
(α_{T})	T0B	0	–	-0.2	-1.0×10^{-1}	$k^0\ \forall\ k$
	T0C	0	–	0.2	1.0×10^{-1}	$k^0\ \forall\ k$
	T0D	0	–	0.5	2.5×10^{-1}	$k^0\ \forall\ k$
Choice 0	M0A	-0.5	–	0	3.3×10^{7}	$k_{\mathrm{IR}}^{-2}\ \&\ k_{\mathrm{UV}}^{0}$
(α_{M})	M0B	-0.3	–	0	3.2×10^{4}	$k_{\mathrm{IR}}^{-2}\ \&\ k_{\mathrm{UV}}^{0}$
	M0C	-0.1	–	0	3.1×10^{1}	$k_{\mathrm{IR}}^{-2}\ \&\ k_{\mathrm{UV}}^{0}$
	M0D	-0.01	–	0	4.1×10^{-1}	$k_{\mathrm{IR}}^{-2}\ \&\ k_{\mathrm{UV}}^{0}$
	M0E	0.1	–	0	-9.7×10^{-1}	$k^0\ \forall\ k$
	M0F	0.3	–	0	-1.0×10^{0}	$k^0\ \forall\ k$
Choice I	M1A	-0.5	2	0	2.5×10^{-1}	$k^0\ \forall\ k$
(α_{M})	M1B	-0.3	2	0	1.5×10^{-1}	$k^0\ \forall\ k$
	M1C	-0.1	2	0	4.7×10^{-2}	$k^0\ \forall\ k$
	M1D	0.1	0.4	0	-2.2×10^{-1}	$k^0\ \forall\ k$
	M1E	0.3	0.4	0	-5.2×10^{-1}	$k^0\ \forall\ k$
Choice II	M2A	-0.5	–	0	2.9×10^{-1}	$k^0\ \forall\ k$
(α_{M})	M2B	-0.3	–	0	1.6×10^{-1}	$k^0\ \forall\ k$
	M2C	-0.1	–	0	5.3×10^{-2}	$k^0\ \forall\ k$
	M2D	0.1	–	0	-5.0×10^{-2}	$k^0\ \forall\ k$
	M2E	0.3	–	0	-1.4×10^{-1}	$k^0\ \forall\ k$
Choice III	M3A	-0.5	–	0	3.5×10^{8}	$k_{\mathrm{IR}}^{-2}\ \&\ k_{\mathrm{UV}}^{0}$
(α_{M})	M3B	-0.3	–	0	1.3×10^{5}	$k_{\mathrm{IR}}^{-2}\ \&\ k_{\mathrm{UV}}^{0}$
	M3C	-0.1	–	0	5.0×10^{1}	$k_{\mathrm{IR}}^{-2}\ \&\ k_{\mathrm{UV}}^{0}$
	M3D	-0.01	–	0	4.8×10^{-1}	$k_{\mathrm{IR}}^{-2}\ \&\ k_{\mathrm{UV}}^{0}$
	M3E	0.1	–	0	-9.8×10^{-1}	$k^0\ \forall\ k$
	M3F	0.3	–	0	-1.0×10^{0}	$k^0\ \forall\ k$

Table 1: Parameters used for the numerical studies: for all runs, $k_1 = 10^{-3}$ is the smallest wave number and $N = 46\,000$ is the number of grid points in one dimension. $\Delta\mathcal{E}_{\mathrm{GW}}/\mathcal{E}_{\mathrm{GW}} \equiv (\mathcal{E}_{\mathrm{GW}} - \mathcal{E}_{\mathrm{GW}}^{\mathrm{GR}})/\mathcal{E}_{\mathrm{GW}}^{\mathrm{GR}}$ indicates the relative changes to the total energy density at the present time. In the last column, we briefly state the changes in the final energy spectrum represented by $\xi(k)$, such that $\Omega_{\mathrm{GW}}(k) \propto \xi(k)\Omega_{\mathrm{GW}}^{\mathrm{GR}}(k)$.

yields the values of a_* and $\mathcal{H}_*$ in equations (2.14) and (2.15). With these values, we can then solve equation (2.4) in units of the normalized time $\eta\mathcal{H}_*$, by mapping the parameterizations in equation (4.1) $\alpha_{\mathrm{M}}(\eta) \to \alpha_{\mathrm{M}}(\eta/\eta_*)$ and using the results from Friedmann equations for $\mathcal{H}$ and a''/a (which are already normalized since a' is computed as the derivative with respect to $\eta\mathcal{H}_*$), given in equation (2.11). The effects on $S_{h'}(k,\eta)$ of the specific choice of the time at which the GWs are generated only appear via the relative magnitude of the terms a''/a and α_{M}' that involve time derivatives (normalized by $\mathcal{H}_*$) compared to k. These terms have been parameterized in equations (3.11) and (4.3), respectively, and their magnitude has been discussed. We have shown that the term a''/a can only induce modifications to the solution at scales several orders of magnitude above the horizon scale, while α_{M}' is only of the order of α_{M} for choice III (see section 4) at very late times within the RD era. For other choices of $\alpha_{\mathrm{M}}(\eta)$, either $\alpha_{\mathrm{M}}' = 0$ (choice 0) or α_{M} itself is orders of magnitude below its present-time value

$\alpha_{M,0}$ (choices I and II). We find that the WKB approximation is expected to be valid around $k \gg k_{\lim, \alpha_M} \sim \sqrt{|\alpha_M^*|/2}$ and, on the other hand, it predicts an enhancement $\xi(k) = k^{-2}$ in the IR regime $k \lesssim k_{\rm crit} \leq k_{\lim, \alpha_M}$, which is not on the range of validity of the WKB estimate. However, we characterize $\xi(k)$ using numerical simulations and we find an IR enhancement $\xi(k) \propto k^{-2}$ that does not in general follow the spectral shape predicted by WKB and that can become shallower at smaller k.

The position of this spectral change is a fixed fraction of the Hubble horizon at the time of generation, determined by the value of α_M^*, that does not depend on the specific value of η_*. Finally, the time of generation determines the range of frequencies where we observe the signal as well as its amplitude via equation (3.15).

The peak amplitude $S_{h'}^*$ can be chosen to represent a specific model. For example, a value of $S_{h'}^* = 3.5 \times 10^{-10}$ is used in our runs (see table 1) and it would produce a normalized initial total energy density[7] $\mathcal{E}_{\rm GW}^* \simeq 10^{-9}$, which corresponds to a vortically turbulent source energy density of roughly $\mathcal{E}_{\rm turb}^* \simeq 3q^{-1} \times 10^{-4}$. This is related via

$$\mathcal{E}_{\rm GW}^* = (q\mathcal{E}_{\rm turb}^*/k_*)^2, \tag{5.3}$$

where q is an empirically determined coefficient for a specific type of turbulence source $\mathcal{E}_{\rm turb}^*$, and is found to be of the order of unity or larger (up to ~ 5), depending on the production mechanism of the source [47? ?].

5.2 Time evolution

For constant $\alpha_T \neq 0$ and $\alpha_M = 0$, the GW energy density stays constant in time and its magnitude is modified by the specific value of α_T, as it can be predicted from the analytical solution to equation (2.4) in the absence of sources during RD, given in equations (3.9) and (3.19) under the WKB approximation. We find excellent agreement between the WKB estimate and the numerical solution of the GW spectra, enhanced by a factor $1 + \frac{1}{2}\alpha_T$. Note that this corresponds to a boost of energy for $\alpha_T > 0$ and a depletion for $\alpha_T < 0$. The relative changes upon the GR solutions are of order $\alpha_T \sim \mathcal{O}(10^{-1})$ (see table 1), which are much larger than the constraint $\alpha_{T,0} \lesssim \mathcal{O}(10^{-15})$. Therefore, the changes due to realistic values of α_T on the total GW energy density are negligible.

Figure 3 presents the time evolution of the total GW energy density $\mathcal{E}_{\rm GW}(\eta)$ of the runs in series M0 (upper left), M1 (upper right), M2 (lower left), and M3 (lower right). In these runs, α_M follows each of the parameterizations given in equation (4.1) and $\alpha_T = 0$. The numerical solutions (dashed lines) and the WKB approximations (solid lines) agree on the total GW energy density time dependence, enhanced or depleted by a factor $e^{-2\mathcal{D}}$. Regardless of the specific parameterization, we find an enhancement or a suppression of $\mathcal{E}_{\rm GW}$ over time for negative or positive values of $\alpha_{M,0}$, respectively.

Choices 0 and III yield similar results, with a time evolution $\mathcal{E}_{\rm GW}(\eta) \sim \eta^{-\alpha_{M,0}}$ and $\mathcal{E}_{\rm GW}(\eta) \sim \eta^{-1.5\,\alpha_{M,0}}$ during RD era, and $\mathcal{E}_{\rm GW} \sim \eta^{-2\alpha_{M,0}}$ and $\mathcal{E}_{\rm GW}(\eta) \sim \eta^0$ during MD, respectively. This agrees with the expectation since choice III mostly differs from choice 0 during MD. During RD, both parameterizations are almost the same and just differ by a factor $1/(1 - \Omega_{\rm mat,0}) \simeq 1.46$, leading to the different scalings. In other words, the evolution

---

[7] The turbulent and GW energy densities are normalized to the radiation energy density, such that $\mathcal{E}_{\rm GW}$ during RD can be computed as
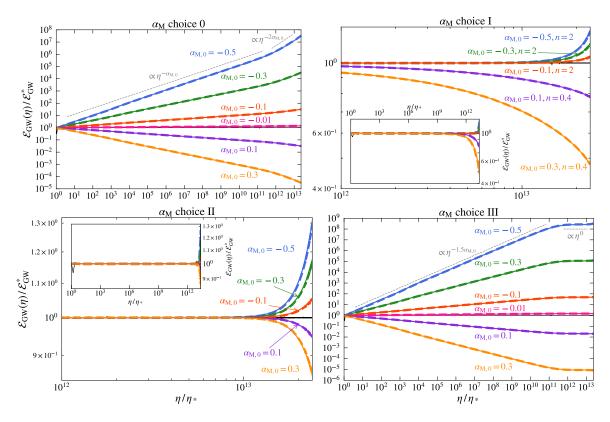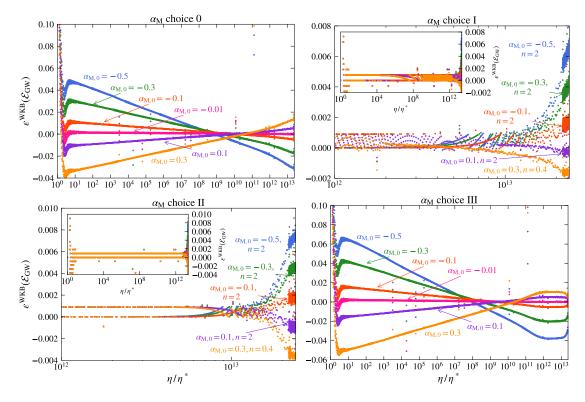
$$\mathcal{E}_{\rm GW}(\eta) = \frac{1}{6} \int_0^\infty S_{h'}(k, \eta)\, {\rm d}k. \tag{5.2}$$

Figure 3: Time evolution of the total energy density $\mathcal{E}_{\rm GW}$. On the upper right panel, solid and dashed curves respectively indicate $\alpha_{\rm M}$ choice 0 and III, which overlap completely. The two lower panels show the evolution during ΛD, with the corresponding insets showing the full evolution. In all panels, the WKB estimate is shown as square dots and the GR solution as the black solid line. All runs are initialized at EWPT such that the present day is represented by $\eta_0/\eta_* \simeq 2.38 \times 10^{13}$.

of $\mathcal{E}_{\rm GW}$, proportional to $a^{-\alpha_{\rm M}}$ when $\alpha_{\rm M}$ is constant (e.g., for choice 0, and for choice III during RD era), is determined by the cosmic expansion itself. Note that choices 0 and III induce an enhancement or suppression in the total energy, $\Delta\mathcal{E}_{\rm GW}/\mathcal{E}_{\rm GW} \equiv (\mathcal{E}_{\rm GW} - \mathcal{E}_{\rm GW}^{\rm GR})/\mathcal{E}_{\rm GW}^{\rm GR}$, that heavily depends on the values of $\alpha_{\rm M,0}$, i.e., $\Delta\mathcal{E}_{\rm GW}/\mathcal{E}_{\rm GW}$ can range from $\mathcal{O}(10^{-1})$ at $\alpha_{\rm M,0} = -0.01$ to $\mathcal{O}(10^7)$ (choice 0) and $\mathcal{O}(10^8)$ (choice III) with $\alpha_{\rm M,0} = -0.5$. In general, choice III leads to a larger enhancement due to larger values of $\alpha_{\rm M}$ during RD than choice 0. The potential implications of such a large GW energy density enhancement are discussed in section 6.

For both choices I and II (see the upper right and lower left panels of figure 3), the modified GW solutions remain close to their GR counterparts for most of the time, and rapidly depart from GR as η enters ΛD and approaches the present day. This is expected since $\alpha_{\rm M}$ is proportional to the scale factor and the dark energy density for choices I and II, respectively, and hence, the values of $\alpha_{\rm M}$ are negligibly small for most of the cosmic history until ΛD era. For this reason, for the same values of $\alpha_{\rm M,0}$, the final values of $\mathcal{E}_{\rm GW}$ in both of these cases are significantly lower than those in choices 0 and III, where the modifications are accumulated from RD onward.

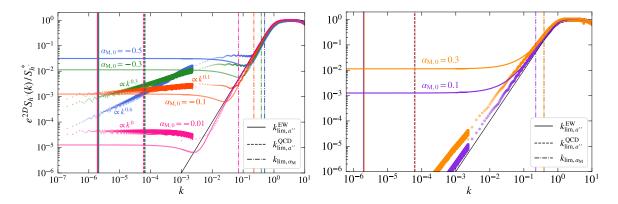In figure 3, the differences between the WKB and the numerical solutions are indis-

Figure 4: Relative error on the time series of the WKB approximation compared to the numerical simulations, $\varepsilon^{\mathrm{WKB}}(\mathcal{E}_{\mathrm{GW}})$.

tinguishable. We quantify in figure 4 the relative error between the two, defined to be $\varepsilon^{\mathrm{WKB}}(\mathcal{E}_{\mathrm{GW}}) \equiv [\mathcal{E}_{\mathrm{GW}}^{\mathrm{WKB}}(\eta) - \mathcal{E}_{\mathrm{GW}}(\eta)]/\mathcal{E}_{\mathrm{GW}}(\eta)$. In all panels, there exists a brief but relative large error region, amounting to $\lesssim 10\%$, around the initial time η_*. This is due to the sinusoidal oscillations of each k mode that are present in GR and modified gravity alike [see equations (3.7) and (3.8)]. After the initial oscillations settle down, $\varepsilon^{\mathrm{WKB}}(\mathcal{E}_{\mathrm{GW}})$ for choices 0 and III decrease over the majority of time in RD. Although they both increase somewhat later on, the maximum error at the final time is only $\varepsilon^{\mathrm{WKB}}(\mathcal{E}_{\mathrm{GW}}) \sim 3\%$. For choices I and II, due to the negligible impact of α_{M} during RD, the GW solutions settle down to the same magnitude after the initial oscillations. Therefore, the relative errors during RD remain zero. During ΛD, the errors grow as the effects of α_{M} become more significant. But this is also limited, since at most $\varepsilon^{\mathrm{WKB}}(\mathcal{E}_{\mathrm{GW}}) \lesssim 1\%$ is found at the present day, lower than in choices 0 and III.

5.3 Energy spectrum

In figure 5, we show the final energy spectrum normalized against the initial amplitude $S_{h'}^*$ and compensated by the factor $e^{-2\mathcal{D}}$ to study the changes on the spectral shape. The saturated spectra, averaged over oscillations at late times, are shown for the choice 0 of α_{M} parameterization, since the results from choice III exhibit similar spectral features, and the rest of runs (α_{T} choice 0, α_{M} choices I and II) show the same spectral slopes as in GR. As a reminder of the potential limitations of WKB approximation, we mark with vertical lines the values of $k_{\mathrm{lim},a''}^{\mathrm{EW}}$ (solid), $k_{\mathrm{lim},a''}^{\mathrm{QCD}}$ (dashed), and $k_{\mathrm{lim},\alpha_{\mathrm{M}}}$ (dash-dotted). We note that $k_{\mathrm{lim},\alpha_{\mathrm{M}}}$ occurs at wave numbers larger than the IR regime characterized by k_{crit}. This implies that

Figure 5: Saturated final energy spectra compensated by the growth on the total GW energy density $e^{2\mathcal{D}}S_{h'}(k)/S_{h'}^*$ for the runs with the choice 0 of α_{M} parameterization. Left and right panels represent negative and positive values of $\alpha_{\mathrm{M},0}$, respectively. The GR solution is shown in black, while the dashed and dotted curves are the WKB approximation and numerical solutions, respectively. Vertical dotted lines indicate the corresponding $k_{\mathrm{lim},\alpha_{\mathrm{M}}}$.
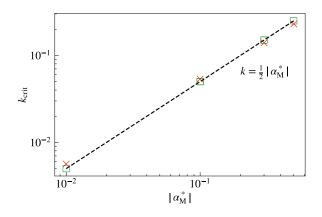

Figure 6: Relation between k_{crit} and $|\alpha_{\mathrm{M}}^*|$ found in the numerical simulations (red crosses), compared to the one expected from the WKB approximation (green squares).

the analytically calculated values of $k_{\mathrm{crit}} = |\alpha_{\mathrm{M}}^*|/2$ can potentially be unreliable. However, figure 6 demonstrates that k_{crit} is numerically found to coincide with the analytic estimations very well.

Comparing the numerical results to the expected spectra obtained using the WKB approximation [see figure 2], we note two main differences. In the first place, the IR enhancement found under the WKB approximation only appears for negative values of $\alpha_{\mathrm{M},0}$ whereas for positive values there are no significant modifications to the spectral shape. In addition, the modifications to the spectral shape are slightly different to those predicted by the WKB estimate. At wave numbers close to where the IR regime starts, $k \lesssim k_{\mathrm{crit}}$, the k^{-2} enhancement is reproduced by the numerical results, flattening that part of the original GR spectrum to k^0. But as k decreases, $k \ll k_{\mathrm{crit}}$, the numerical spectra exhibit slopes steeper than k^0 that is not predicted by the WKB approximation, which maintains the k^0 slope throughout all scales $k \le k_{\mathrm{crit}}$. The departure in the IR regime occurs at different scales depending on the values of $\alpha_{\mathrm{M},0}$. For $\alpha_{\mathrm{M},0} = -0.01$, this is the least obvious, where the enhanced spectrum still keeps a roughly k^0 shape even at $k \ll k_{\mathrm{crit}}$. For $\alpha_{\mathrm{M},0} = -0.5$, however, the difference
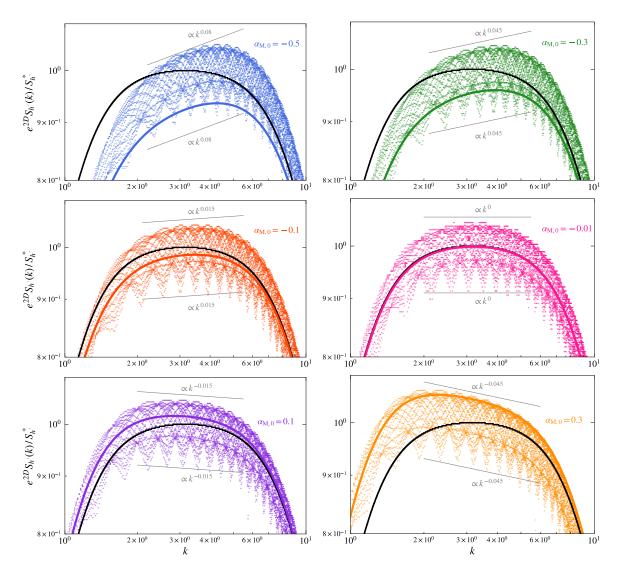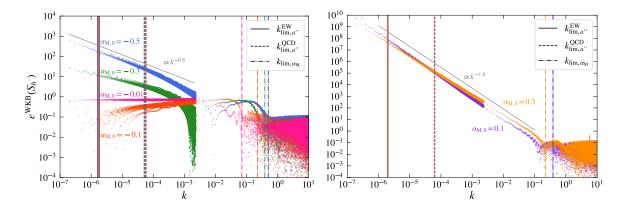
Figure 7: Saturated final energy spectra around between $k_{\rm b}$ and $k_{\rm peak}$. In all panels, numerical results are represented by scattered dots, WKB approximation is shown in solid curves, and GR solution is in black.

becomes visible when k is still relatively close to the start of the IR regime at $k \sim k_{\rm crit}$.

In figure 7, we inspect the modified spectra between $k_{\rm b}$ and $k_{\rm peak}$, where the thick solid lines are from WKB approximation [recall the inset of figure 2]. In terms of the spectrum amplitudes, for all $\alpha_{\rm M,0} < -0.01$, we see that WKB underestimates in this subrange compared to the numerical results. For $\alpha_{\rm M,0} \geq -0.01$, WKB approximation gradually approaches but does not seem to overshoot the numerical results. In terms of the spectral slopes, both WKB and numerical solutions give the same results for all values of $\alpha_{\rm M,0}$ considered. However, note that the changes in the spectral slopes are extremely small, no more than $k^{0.1}$ for all $|\alpha_{\rm M,0}| < 0.5$.

Finally, to quantify the departures of WKB approximation from numerical solutions, especially at $k \leq k_{\rm lim,\alpha_{\rm M}}$, we show the relative errors in the spectra as $\varepsilon^{\rm WKB}(S_{h'}) \equiv [S_{h'}(k)^{\rm WKB} - S_{h'}(k)]/S_{h'}(k)$ in figure 8, calculated at the present time. We observe that for positive values

Figure 8: Relative error $\varepsilon^{\mathrm{WKB}}(S_{h'})$ in the saturated spectra at late times of the WKB approximation compared to the numerical simulations. The vertical lines correspond to the wave number $k_{\mathrm{lim},\,\alpha_{\mathrm{M}}}$, below which the WKB estimate is expected to break down.

of $\alpha_{\mathrm{M},0}$, the errors grow monotonically as k becomes smaller. In fact, $\varepsilon^{\mathrm{WKB}}(S_{h'}) \sim k^{-2}$ is found due to a consistent disagreement between spectral slopes k^0 predicted by WKB formalism and $\sim k^{-2}$ obtained numerically. On the other hand, for negative values of $\alpha_{\mathrm{M},0}$, $\varepsilon^{\mathrm{WKB}}(S_{h'})$ also increase as k becomes smaller. But since $\alpha_{\mathrm{M},0} < 0$ still produces certain degree of IR enhancement in numerical results, the slope in the error spectrum does not become as steep and depends on the corresponding values of $\alpha_{\mathrm{M},0}$. In both panels of figure 8, however, the errors are limited at $\lesssim 10\%$ above $k_{\mathrm{lim},\,\alpha_{\mathrm{M}}}$.

6 Observational implications

To infer the observational prospects of detecting a modified GWB, we convert the linear energy spectrum $S_{h'}(k)$ directly obtained from the code to the commonly used logarithmic energy spectrum $\Omega_{\mathrm{GW}}(f)$ via equation (3.15). The normalized wave numbers used in the code are converted to the present-day physical frequencies via

$$f = \frac{k\mathcal{H}_*}{2\pi}\left(\frac{a_*}{a_0}\right). \tag{6.1}$$

As a result, the GR solution in the form of the double broken power law used in the numerical simulations, i.e., $S_{h'}(k) \propto k^2$ and $S_{h'}(k) \propto k^{-2}$ in the low- and high wave number regimes, becomes $\Omega_{\mathrm{GW}}(f) \propto f^3$ in the IR and $\Omega_{\mathrm{GW}}(f) \propto f^{-1}$ in the UV regimes, respectively.

   Choosing the cases with the most pronounced modifications, we show in figure **??** the results from series M0, where the solid black curves show GR solutions and colored ones indicate $\alpha_{\mathrm{M},0} = -0.5$ (blue), -0.3 (green), -0.1 (orange), and -0.01 (purple). Assuming QCDPT as the initial time of GW production, the current-day $\Omega_{\mathrm{GW}}(f)$ peaks around the nHz frequency band, shown by the fainter set of colored curves. If instead the initial time is around EWPT, then $\Omega_{\mathrm{GW}}(f)$ today peaks closer to the mHz band, illustrated by the curves in the same but darker colors. For these, we extend further into the IR and UV regimes with dashed lines with slopes f^1 and $f^{-8/3}$, respectively. As a f^2 spectral enhancement upon the f^3 slope of the GR solution in the IR, all curves corresponding to $\alpha_{\mathrm{M},0} < 0$ already exhibit f^1 towards their low-frequency tails. On the other hand, we extend the UV tail with a slope of $f^{-8/3}$, in accordance to what is commonly found for turbulence-induced GWs.
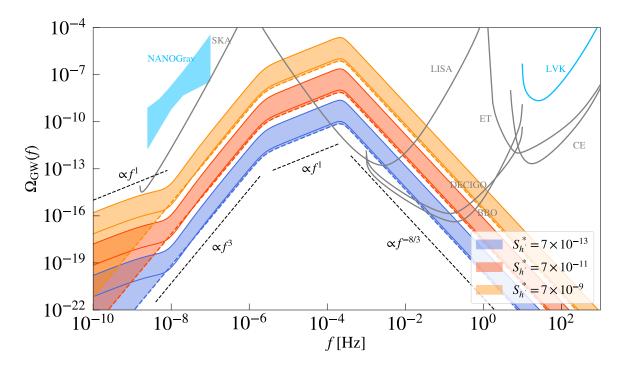
Figure 9: The present-day modified GW energy spectrum for parameter choice 0. Different colors of the shades represent different initial peak amplitude. The shaded regions are bounded by $\alpha_{\mathrm{M},0} = -0.01$ and -0.1. Several detectors' power-law sensitivity (PLS) curves are shown for comparison: SKA, LISA, DECIGO, Big Bang Observatory (BBO), Einstein Telescope (ET), and Cosmic Explorer (CE) are in gray, and NANOGrav and LVK are in light blue. All PLS assumes a signal-to-noise ratio of 10 and an observation time of 4 years.

For observational comparisons, we plot in gray the power law sensitivity (PLS) curves of proposed future detectors such as SKA [44], DECIGO, BBO [?], LISA [46, 47], Einstein Telescope (ET), and Cosmic Explorer (CE) [?]. For current detectors, we show in light blue the 2σ-confidence contour assuming a 30-frequency power law using the NANOGrav 12.5-year dataset [45] and the PLS of the LIGO-Virgo-KAGRA (LVK) [?] network.

There is a number of implications to unfold here. First, assuming a QCDPT origin and a conservative amount of initial GWs at $\mathcal{E}_{\mathrm{GW}}^* \approx 10^{-9}$ (upper panel of figure **??**), $\alpha_{\mathrm{M},0} \gtrsim -0.5$ can already be excluded as it overshoots the NANOGrav contour. Smaller values such as $\alpha_{\mathrm{M},0} = -0.3$ and -0.1 amplify the otherwise unobserved GR solution to the NANOGrav and the expected SKA ranges. Similarly for GWs from the EWPT epoch, $\alpha_{\mathrm{M},0} \lesssim -0.3$ could boost the GR solution, otherwise under the LISA and DECIGO curves, to be above them. Assuming a more optimistic value of $\mathcal{E}_{\mathrm{GW}}^* \approx 10^{-5}$ (lower panel of figure **??**), which could be due to a larger amount of $\mathcal{E}_{\mathrm{M}}^* \approx 10^{-1}$, the constraints are correspondingly stronger. In this case, NANOGrav could rule out $\alpha_{\mathrm{M},0} \gtrsim -0.3$ for GWs from the QCDPT epoch, whereas for GWs from EWPT, a smaller $\alpha_{\mathrm{M},0} \lesssim -0.1$ would be sufficient to boost a GR solution to intersect with LISA and DECIGO detection ranges. Although these amplification effects could in principle provide upper and lower bounds of $|\alpha_{\mathrm{M},0}|$ (for $\alpha_{\mathrm{M},0} < 0$), the present-day amplitude of the GW spectrum is degenerate with respect to the value of $\alpha_{\mathrm{M},0}$ as well as the initial GW amplitude, the latter of which contains a fair amount of uncertainty itself. In addition to the GW amplitude, its spectral peaks and slopes are also crucial factors that

affects the detectability. The discussions here are done rather qualitatively, where we inspect the $f^{-8/3}$ behavior (dashed lines) beyond the peak that, in reality, depends on the nature of the turbulence source. The peak itself, which is assumed to occur at $k_* = 10$ initially, also varies depending on the physics of turbulence after the phase transitions. Therefore, in practice, constraining $|\alpha_{\mathrm{M},0}|$ via its amplification effects can be rather challenging.

On the other hand, $\alpha_{\mathrm{M},0}$ also introduces a spectral enhancement such that $f^3 \to f^1$ in the low-frequency end. Assuming QCDPT as the GW production time, this feature lies below the peak around nHz and thus outside the detectors in that frequency range. Assuming EWPT as the initial time is more interesting, as the spectral enhancement could potentially lift the low-frequency tails up into the nHz range of detectors such as NANOGrav and SKA. Combining the low-frequency spectral enhancement and the overall amplitude boost, certain values of $\alpha_{\mathrm{M},0}$ would be particularly interesting to explore, where the modified GW spectrum could potentially be seen across nHz, mHz, and dHz detection ranges. For example, it could happen for $\alpha_{\mathrm{M},0} \lesssim -0.3$ if $\mathcal{E}_{\mathrm{GW}}^* \approx 10^{-9}$ or $\alpha_{\mathrm{M},0} \lesssim -0.1$ if $\mathcal{E}_{\mathrm{GW}}^* \approx 10^{-5}$. This possibility provides a way to reduce the degeneracy of parameters, especially with regards to the initial GW energy $\mathcal{E}_{\mathrm{GW}}^*$.

Finally, we note that values such as $\alpha_{\mathrm{M},0} = -0.3$ or -0.5 could potentially dominate the sensitivity budget of various detectors, mostly LISA and DECIGO but also SKA and NANOGrav, especially if the GW amplitude $\mathcal{E}_{\mathrm{GW}}^*$ is large to begin with. If this actually happens, then the said detectors would have extreme difficulties extracting subdominant GW signals from other sources such as astrophysical objects, as they do not receive the significant boost accumulated over longer periods of time as cosmological ones do. Therefore, an upper bound could also be placed on $|\alpha_{\mathrm{M},0}|$ in the event that GWs from closer-by astrophysical sources are identified by, for example, LISA.

7   Conclusions

GWs in modified gravity theories exhibit features in their energy spectra different from what can be expected from GR. We explored the significance of such features in terms of the spectral slopes and amplitudes in different frequency ranges, under different functional forms and values of two modification parameters – the running of effective Planck mass α_{M} and the tensor speed excess α_{T}. We also compared the analytical WKB approximation and numerical solutions and found that the former is not always in agreement with the latter, especially in the low-frequency regimes at late times.

The current-day value of α_{T} is already tightly constrained. In this paper we further found the relatively insignificant modifications introduced by α_{T}, even if taken to be unphysically large values compared to its constraint. On the other hand, α_{M} acts as an (anti-)damping term in the GW equation and can impart changes to the energy spectrum of GWs produced by MHD sources at EWPT and QCDPT with potential implications to future observations, especially in the nHz and mHz frequency ranges.

In principle, the values of α_{M} could be constrained by the spectral shape and amplitude of the GW energy spectrum, especially since $\alpha_{\mathrm{M}} < 0$ flattens the low-frequency tail of the spectrum by a factor of f^2 and boosts the overall amplitude of the spectrum. In practice, this is a rather complex problem with parameter degeneracies, as the un-modified GW spectrum could also have larger or smaller amplitude due to a range of possible source amplitudes to begin with, in addition to the uncertainties of the GW spectral slopes that depend on the physics of turbulence sources after the phase transitions. Combining multiple detectors at dif-

ferent frequency ranges could help reducing the degeneracy. Identifying astrophysical sources could also put constraints on $\alpha_{\rm M}$. But overall, we provide a rather qualitative discussion here and the utilization of GW spectrum from early-universe sources as a probe of the parameter $\alpha_{\rm M}$ requires more detailed studies on various aspects of the subject.

Data availability. The source code used for the numerical solutions of this study, the PENCIL CODE, is freely available [27]; see also ref. [48] for the numerical data.

Acknowledgments

A Numerical scheme

Similar to what has been done in refs. [28, 49], we implement a matrix solver for the modified GW equation. We start by simplifying the notations in equation (2.4) as

$$h'' + \sigma h' + \omega^2 h = \mathcal{G} T, \tag{A.1}$$

where $\mathcal{G} \equiv 6/a(\eta)$, and

$$\sigma \equiv \alpha_{\rm M} \mathcal{H}, \ \ \omega^2 \equiv c_{\rm T}^2 k^2 - \alpha_{\rm M} \mathcal{H}^2 - \frac{a''}{a}. \tag{A.2}$$

Then from the characteristic equation

$$\lambda^2 + \sigma\lambda + \omega^2 = 0, \tag{A.3}$$

the eigenvalues λ can be obtained as

$$\lambda_{1,2} = -\frac{1}{2}\left(\sigma \mp \sqrt{\sigma^2 - 4\omega^2}\right). \tag{A.4}$$

For $\delta\eta \ll 1$, we assume $T_{(\eta)} \approx T_{(\eta+\delta\eta)}$, which is justified when considering MHD sources as their characteristic time scales are typically much shorter than those of GWs, and $\lambda'_{1,2} \approx \lambda''_{1,2} \approx 0$. Then solutions for the strain quantities in equation (A.1) take the form of

$$h_{(\eta+\delta\eta)} - \omega^{-2}\mathcal{G} T_{(\eta+\delta\eta)} = \mathcal{C} e^{\lambda_1\delta\eta} + \mathcal{D} e^{\lambda_2\delta\eta} \tag{A.5}$$

$$h'_{(\eta+\delta\eta)} = \mathcal{C}\lambda_1 e^{\lambda_1\delta\eta} + \mathcal{D}\lambda_2 e^{\lambda_2\delta\eta}, \tag{A.6}$$

where $\mathcal{C}$ and $\mathcal{D}$ are constant amplitude coefficients evaluated at η. Equivalently in matrix form for h and h', the solutions can be rewritten as

$$\begin{pmatrix} \omega h - \omega^{-1}\mathcal{G} T \\ h' \end{pmatrix}_{\eta+\delta\eta} = \begin{pmatrix} \omega e^{\lambda_1\delta\eta} & \omega e^{\lambda_2\delta\eta} \\ \lambda_1 e^{\lambda_1\delta\eta} & \lambda_2 e^{\lambda_2\delta\eta} \end{pmatrix} \begin{pmatrix} \mathcal{C} \\ \mathcal{D} \end{pmatrix}. \tag{A.7}$$

So the amplitude coefficients can be obtained as

$$
\begin{pmatrix} \mathcal{C} \\ \mathcal{D} \end{pmatrix} = \begin{pmatrix} \omega e^{\lambda_1 \delta\eta} & \omega e^{\lambda_2 \delta\eta} \\ \lambda_1 e^{\lambda_1 \delta\eta} & \lambda_2 e^{\lambda_2 \delta\eta} \end{pmatrix}^{-1} \begin{pmatrix} \omega h - \omega^{-1}\mathcal{G}T \\ h' \end{pmatrix}_{\eta+\delta\eta} \tag{A.8}
$$

$$
= \frac{1}{\omega(\lambda_2 - \lambda_1)e^{(\lambda_1+\lambda_2)\delta\eta}} \begin{pmatrix} \lambda_2 e^{\lambda_2 \delta\eta} & -\omega e^{\lambda_2 \delta\eta} \\ -\lambda_1 e^{\lambda_1 \delta\eta} & \omega e^{\lambda_1 \delta\eta} \end{pmatrix} \begin{pmatrix} \omega h - \omega^{-1}\mathcal{G}T \\ h' \end{pmatrix}_{\eta+\delta\eta} \tag{A.9}
$$

$$
\lim_{\delta\eta\to 0} \begin{pmatrix} \mathcal{C} \\ \mathcal{D} \end{pmatrix} = \frac{1}{\omega(\lambda_2 - \lambda_1)} \begin{pmatrix} \lambda_2 & -\omega \\ -\lambda_1 & \omega \end{pmatrix} \begin{pmatrix} \omega h - \omega^{-1}\mathcal{G}T \\ h' \end{pmatrix}_{\eta,} \tag{A.10}
$$

where, in the last step, we used the fact that $\mathcal{C},_\mathcal{D}$ are time-independent. Therefore, the time evolution of the relevant quantities can be obtained via a matrix multiplication as

$$
\begin{pmatrix} \omega h - \omega^{-1}\mathcal{G}T \\ h' \end{pmatrix}_{\eta+\delta\eta} = \mathcal{M} \begin{pmatrix} \omega h - \omega^{-1}\mathcal{G}T \\ h' \end{pmatrix}_{\eta,} \tag{A.11}
$$

where

$$
\mathcal{M} = \frac{1}{\lambda_1 - \lambda_2} \begin{pmatrix} \lambda_1 e^{\lambda_2 \delta\eta} - \lambda_2 e^{\lambda_1 \delta\eta} & \omega(e^{\lambda_1 \delta\eta} - e^{\lambda_2 \delta\eta}) \\ \omega^{-1}\lambda_1\lambda_2(e^{\lambda_2 \delta\eta} - e^{\lambda_1 \delta\eta}) & \lambda_1 e^{\lambda_1 \delta\eta} - \lambda_2 e^{\lambda_2 \delta\eta} \end{pmatrix}. \tag{A.12}
$$

In the case of $\sigma = 0, \omega^2 = k^2$, the eigenvalues become $\lambda_{1,2} = \pm ik$ and the evolution matrix reduces to

$$
\mathcal{M} = \begin{pmatrix} \cos k\delta\eta & \sin k\delta\eta \\ -\sin k\delta\eta & \cos k\delta\eta \end{pmatrix}. \tag{A.13}
$$

Note that so far these are written in line with the convention of ref. [28]. However, in the PENCIL CODE [27], the relevant evolution equation [equation (A.11)] is implemented as

$$
\begin{pmatrix} h - \omega^{-2}\mathcal{G}T \\ \omega^{-1}h' \end{pmatrix}_{\eta+\delta\eta} = \mathcal{M} \begin{pmatrix} h - \omega^{-2}\mathcal{G}T \\ \omega^{-1}h' \end{pmatrix}_{\eta,} \tag{A.14}
$$

where $\mathcal{M}$ is the same as in equation (A.12).

B   Numerical accuracy

Accuracy as a function of time intervals

In this section we attach a few case studies on numerical accuracy. Although the GW solver in the PENCIL CODE has been made accurate to second order in time, this is only true when the coefficients are constant in time. When the coefficients vary only slowly, the error is also small, but depends on the length of the time step only to first order. This is demonstrated in figure 10, where we show on the left panel the relative errors in the GW energy during RD and MD, and on the right panel that during ΛD. Recall that during RD and MD, we use increasing time steps, represented by n_{incr} here. During ΛD, we revert back to linear time steps, with the interval shown as η_{incr} in figure 10. Another way of seeing the time accuracy is via figure 11, where we show the final energy spectrum (left panel) and its averaged results (right panel) for run M0A. Different colors indicate the linear time intervals during ΛD and the black curves are the spectrum obtained by running M0A entirely with increasing time
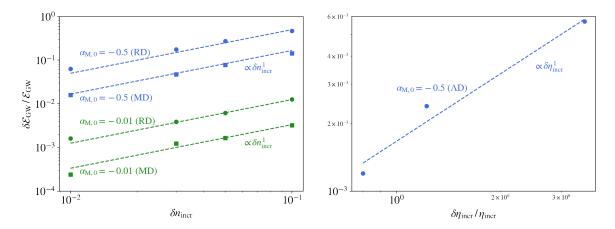
Figure 10: Relative errors as a function of time intervals. *Left panel*: The accuracy during RD (round dots) and MD (square dots) for $\alpha_{\mathrm{M},0} = -0.5$ (blue) and $\alpha_{\mathrm{M},0} = -0.01$ (green), where δn_{incr} is the difference in the time steps. *Right panel*: $\delta\eta_{\mathrm{incr}}$ indicates the linear time interval difference during ΛD.
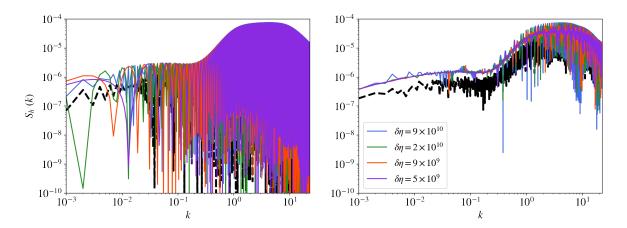

Figure 11: Final energy spectrum $E_{\mathrm{GW}}(k)$ (left) and the averaged results (right) for $\alpha_{\mathrm{M},0} = -0.5$ (run M0A). All runs are done with increasing time steps using $n_{\mathrm{incr}} = 0.01$ during RD and MD but continue in linear time intervals (indicated by the colors) during ΛD. The black dashed curves being the run M0A done entirely with increasing time steps with $n_{\mathrm{incr}} = 0.01$.

steps using $n_{\mathrm{incr}} = 0.01$. In other words, the colored curves only differ from the black one from the linear time stepping during ΛD. We observe that all chosen values of $\delta\eta$ produce converging energy spectra in the small-k regime after averaging, although larger values of $\delta\eta$ result in more fluctuations in the un-averaged spectra. We also note that, compared to results from hybrid time steps, the entirely nonuniform time steps underestimate the final energy spectrum.

References

[1] A.G. Riess, S. Casertano, W. Yuan, L.M. Macri and D. Scolnic, *Large Magellanic Cloud Cepheid Standards Provide a 1% Foundation for the Determination of the Hubble Constant and Stronger Evidence for Physics beyond ΛCDM, Astrophys. J.* **876** (2019) 85 [1903.07603].

[2] A.G. Riess, S. Casertano, W. Yuan, J.B. Bowers, L. Macri, J.C. Zinn et al., *Cosmic Distances Calibrated to 1% Precision with Gaia EDR3 Parallaxes and Hubble Space Telescope Photometry of 75 Milky Way Cepheids Confirm Tension with ΛCDM*, *Astrophys. J. Lett.* **908** (2021) L6 [2012.08534].

[3] A.G. Riess et al., *A Comprehensive Measurement of the Local Value of the Hubble Constant with 1 km s^{-1} Mpc^{-1} Uncertainty from the Hubble Space Telescope and the SHOES Team*, *Astrophys. J. Lett.* **934** (2022) L7 [2112.04510].

[4] K.C. Wong et al., *H0LiCOW – XIII. A 2.4 per cent measurement of H0 from lensed quasars: 5.3σ tension between early- and late-Universe probes*, *Mon. Not. Roy. Astron. Soc.* **498** (2020) 1420 [1907.04869].

[5] D.W. Pesce et al., *The Megamaser Cosmology Project. XIII. Combined Hubble constant constraints*, *Astrophys. J. Lett.* **891** (2020) L1 [2001.09213].

[6] PLANCK collaboration, *Planck 2018 results. VI. Cosmological parameters*, *Astron. Astrophys.* **641** (2020) A6 [1807.06209].

[7] BOSS collaboration, *The clustering of galaxies in the completed SDSS-III Baryon Oscillation Spectroscopic Survey: cosmological analysis of the DR12 galaxy sample*, *Mon. Not. Roy. Astron. Soc.* **470** (2017) 2617 [1607.03155].

[8] L. Verde, T. Treu and A.G. Riess, *Tensions between the Early and the Late Universe*, *Nature Astron.* **3** (2019) 891 [1907.10625].

[9] S. Joudaki et al., *KiDS-450 + 2dFLenS: Cosmological parameter constraints from weak gravitational lensing tomography and overlapping redshift-space galaxy clustering*, *Mon. Not. Roy. Astron. Soc.* **474** (2018) 4894 [1707.06627].

[10] L. Perivolaropoulos and F. Skara, *Challenges for ΛCDM: An update*, *New Astron. Rev.* **95** (2022) 101659 [2105.05208].

[11] D. Lovelock, *The Einstein tensor and its generalizations*, *J. Math. Phys.* **12** (1971) 498.

[12] D. Lovelock, *The four-dimensionality of space and the einstein tensor*, *J. Math. Phys.* **13** (1972) 874.

[13] T. Clifton, P.G. Ferreira, A. Padilla and C. Skordis, *Modified Gravity and Cosmology*, *Phys. Rept.* **513** (2012) 1 [1106.2476].

[14] G.W. Horndeski, *Second-order scalar-tensor field equations in a four-dimensional space*, *Int. J. Theor. Phys.* **10** (1974) 363.

[15] C. Deffayet, X. Gao, D.A. Steer and G. Zahariade, *From k-essence to generalised Galileons*, *Phys. Rev. D* **84** (2011) 064039 [1103.3260].

[16] T. Kobayashi, M. Yamaguchi and J. Yokoyama, *Generalized G-inflation: Inflation with the most general second-order field equations*, *Prog. Theor. Phys.* **126** (2011) 511 [1105.5723].

[17] C. Brans and R.H. Dicke, *Mach's principle and a relativistic theory of gravitation*, *Phys. Rev.* **124** (1961) 925.

[18] B. Ratra and P.J.E. Peebles, *Cosmological Consequences of a Rolling Homogeneous Scalar Field*, *Phys. Rev. D* **37** (1988) 3406.

[19] A. De Felice and S. Tsujikawa, *f(R) theories*, *Living Rev. Rel.* **13** (2010) 3 [1002.4928].

[20] S.M. Carroll, A. De Felice, V. Duvvuri, D.A. Easson, M. Trodden and M.S. Turner, *The Cosmology of generalized modified gravity models*, *Phys. Rev. D* **71** (2005) 063513 [astro-ph/0410031].

[21] C. Armendariz-Picon, V.F. Mukhanov and P.J. Steinhardt, *Essentials of k essence*, *Phys. Rev. D* **63** (2001) 103510 [astro-ph/0006373].

[22] C. Deffayet, O. Pujolas, I. Sawicki and A. Vikman, *Imperfect Dark Energy from Kinetic Gravity Braiding*, *JCAP* **10** (2010) 026 [1008.0048].

[23] A. Nicolis, R. Rattazzi and E. Trincherini, *The Galileon as a local modification of gravity*, *Phys. Rev. D* **79** (2009) 064036 [0811.2197].

[24] M. Petronikolou, S. Basilakos and E.N. Saridakis, *Alleviating H_0 tension in Horndeski gravity*, 2110.01338.

[25] LIGO SCIENTIFIC, VIRGO, FERMI-GBM, INTEGRAL collaboration, *Gravitational Waves and Gamma-rays from a Binary Neutron Star Merger: GW170817 and GRB 170817A*, *Astrophys. J. Lett.* **848** (2017) L13 [1710.05834].

[26] J.M. Ezquiaga and M. Zumalacárregui, *Dark Energy After GW170817: Dead Ends and the Road Ahead*, *Phys. Rev. Lett.* **119** (2017) 251304 [1710.05901].

[27] PENCIL CODE collaboration, *The Pencil Code, a modular MPI code for partial differential equations and particles: multipurpose and multiuser-maintained*, *J. Open Source Softw.* **6** (2021) 2807 [2009.08231].

[28] A. Roper Pol, A. Brandenburg, T. Kahniashvili, A. Kosowsky and S. Mandal, *The timestep constraint in solving the gravitational wave equations sourced by hydromagnetic turbulence*, *Geophys. Astrophys. Fluid Dynamics* **114** (2020) 130 [1807.05479].

[29] H. Takeda, S. Morisaki and A. Nishizawa, *Search for scalar-tensor mixed polarization modes of gravitational waves*, *Phys. Rev. D* **105** (2022) 084019 [2105.00253].

[30] C. Caprini, D.G. Figueroa, R. Flauger, G. Nardini, M. Peloso, M. Pieroni et al., *Reconstructing the spectral shape of a stochastic gravitational wave background with LISA*, *JCAP* **11** (2019) 017 [1906.09244].

[31] E. Bellini and I. Sawicki, *Maximal freedom at minimum cost: linear large-scale structure in general modifications of gravity*, *JCAP* **07** (2014) 050 [1404.3713].

[32] R.C. Nunes, M.E.S. Alves and J.C.N. de Araujo, *Primordial gravitational waves in Horndeski gravity*, *Phys. Rev. D* **99** (2019) 084022 [1811.12760].

[33] Y. He, A. Brandenburg and A. Sinha, *Tensor spectrum of turbulence-sourced gravitational waves as a constraint on graviton mass*, *JCAP* **07** (2021) 015 [2104.03192].

[34] K. Saikawa and S. Shirai, *Primordial gravitational waves, precisely: The role of thermodynamics in the Standard Model*, *JCAP* **05** (2018) 035 [1803.01038].

[35] M.B. Hindmarsh, M. Lüben, J. Lumma and M. Pauly, *Phase transitions in the early universe*, *SciPost Phys. Lect. Notes* **24** (2021) 1 [2008.09136].

[36] A. Nishizawa, *Generalized framework for testing gravity with gravitational-wave propagation. I. Formulation*, *Phys. Rev. D* **97** (2018) 104037 [1710.04825].

[37] S. Arai and A. Nishizawa, *Generalized framework for testing gravity with gravitational-wave propagation. II. Constraints on Horndeski theory*, *Phys. Rev. D* **97** (2018) 104038 [1711.03776].

[38] C. de Rham and S. Melville, *Gravitational Rainbows: LIGO and Dark Energy at its Cutoff*, *Phys. Rev. Lett.* **121** (2018) 221101 [1806.09417].

[39] T. Baker et al., *Measuring the propagation speed of gravitational waves with LISA*, 2203.00566.

[40] L. Lombriser and A. Taylor, *Breaking a Dark Degeneracy with Gravitational Waves*, *JCAP* **03** (2016) 031 [1509.08458].

[41] S.D. Odintsov, V.K. Oikonomou and R. Myrzakulov, *Spectrum of Primordial Gravitational Waves in Modified Gravities: A Short Overview*, *Symmetry* **14** (2022) 729 [2204.00876].

[42] J. Kennedy, L. Lombriser and A. Taylor, *Reconstructing Horndeski theories from phenomenological modified gravity and dark energy models on cosmological scales*, *Phys. Rev. D* **98** (2018) 044051 [1804.04582].

[43] J. Gleyzes, *Parametrizing modified gravity for cosmological surveys*, *Phys. Rev. D* **96** (2017) 063516 [1705.04714].

[44] M. Denissenya and E.V. Linder, *Gravity's Islands: Parametrizing Horndeski Stability*, *JCAP* **11** (2018) 010 [1808.00013].

[45] M. Yoshimura, *Stronger gravity in the early universe*, 2204.11384.

[46] M. Zumalacarregui, *Gravity in the Era of Equality: Towards solutions to the Hubble problem without fine-tuned initial conditions*, *Phys. Rev. D* **102** (2020) 023523 [2003.06396].

[47] M. Braglia, M. Ballardini, F. Finelli and K. Koyama, *Early modified gravity in light of the H_0 tension and LSS data*, *Phys. Rev. D* **103** (2021) 043528 [2011.12934].

[48] E.V. Linder, *Gravitational Wave Distances in Horndeski Cosmology*, 2108.11526.

[49] A. Roper Pol, S. Mandal, A. Brandenburg, T. Kahniashvili and A. Kosowsky, *Numerical simulations of gravitational waves from early-universe turbulence*, *Phys. Rev. D* **102** (2020) 083512 [1903.08585].

[50] A. Roper Pol, C. Caprini, A. Neronov and D. Semikoz, *Gravitational wave signal from primordial magnetic fields in the Pulsar Timing Array frequency band*, *Phys. Rev. D* **105** (2022) 123502 [2201.05630].

[51] M. Hindmarsh and M. Hijazi, *Gravitational waves from first order cosmological phase transitions in the Sound Shell Model*, *JCAP* **12** (2019) 062 [1909.10040].

[52] A. Brandenburg, G. Gogoberidze, T. Kahniashvili, S. Mandal, A. Roper Pol and N. Shenoy, *The scalar, vector, and tensor modes in gravitational wave turbulence simulations*, *Class. Quant. Grav.* **38** (2021) 145002 [2103.01140].

[53] A. Roper Pol, S. Mandal, A. Brandenburg and T. Kahniashvili, *Polarization of gravitational waves from helical MHD turbulent sources*, *JCAP* **04** (2022) 019 [2107.05356].

[54] C.J. Moore, R.H. Cole and C.P.L. Berry, *Gravitational-wave sensitivity curves*, *Class. Quant. Grav.* **32** (2015) 015014 [1408.0740].

[55] K. Schmitz, *New Sensitivity Curves for Gravitational-Wave Signals from Cosmological Phase Transitions*, *JHEP* **01** (2021) 097 [2002.04615].

[56] NANOGrav collaboration, *The NANOGrav 12.5 yr Data Set: Search for an Isotropic Stochastic Gravitational-wave Background*, *Astrophys. J. Lett.* **905** (2020) L34 [2009.04496].

[57] Y. He, A. Roper Pol and A. Brandenburg, *Datasets of "Modified propagation of gravitational waves from the early radiation era"*, *doi: 10.5281/zenodo.7327770 (v2022.11.16); see also* `http://norlx65.nordita.org/~yutong/projects/Horndeski/` *for easier access, .*

[58] A. Brandenburg and R. Sharma, *Simulating Relic Gravitational Waves from Inflationary Magnetogenesis*, *Astrophys. J.* **920** (2021) 26 [2106.03857].